

RESEARCH

Open Access



Arhgef7 as a key target for enriched environment rescuing spatial cognitive deficits and anxiety-like behaviors in a mouse model of Alzheimer's disease following early social isolation

Yimiao Wang^{1†}, Ze Wang^{1,2†}, Yue Li¹, Min Cao¹, Shuying Zhang¹, Shixin Ding¹, Sijia Chen¹, Yuxi Jin¹, Yanli Zhang^{1*}, Junying Gao^{1*} and Ming Xiao^{1,2*}

Abstract

Background Both social and physical environmental factors influence the progression of Alzheimer's disease (AD), but the underlying mechanisms are not yet fully understood. This study aims to investigate how an enriched environment (EE) alleviates the detrimental effects of early social isolation (SI) on AD-like pathophysiology.

Methods Four-week-old 5×FAD transgenic mice were randomly divided into group-housed and isolated groups. After 3 weeks, the mice were further raised in either a physical EE or a standard environment for an additional 3 weeks. Subsequently, these experimental subjects underwent a two-week of behavioral tests while maintaining their original housing conditions unchanged, followed by neuropathological analyses. A series of experiments were conducted on the medial prefrontal cortex (mPFC), including transcriptome sequencing, cellular localization, and knockdown and overexpression of a candidate gene, to identify the key molecules through which physical EE alleviates SI-induced AD-like alterations. The protective effects of the identified gene on cultured forebrain neurons exposed to β -amyloid stimulation, as well as its associated signaling pathways, were also investigated.

Results EE enhanced cognitive function and alleviated anxiety-like behavior in SI-5×FAD mice, partially reversing dendritic and synaptic loss and glial cell activation in the mPFC. However, it did not mitigate deficits in social and cooperative behaviors, hypomyelination, or β -amyloid deposition. Notably, group-housed 5×FAD mice raised in the EE exhibited alleviation of the aforementioned AD-like phenotypes. Transcriptomic and bioinformatic analyses

[†]Yimiao Wang and Ze Wang contributed equally to this work.

*Correspondence:

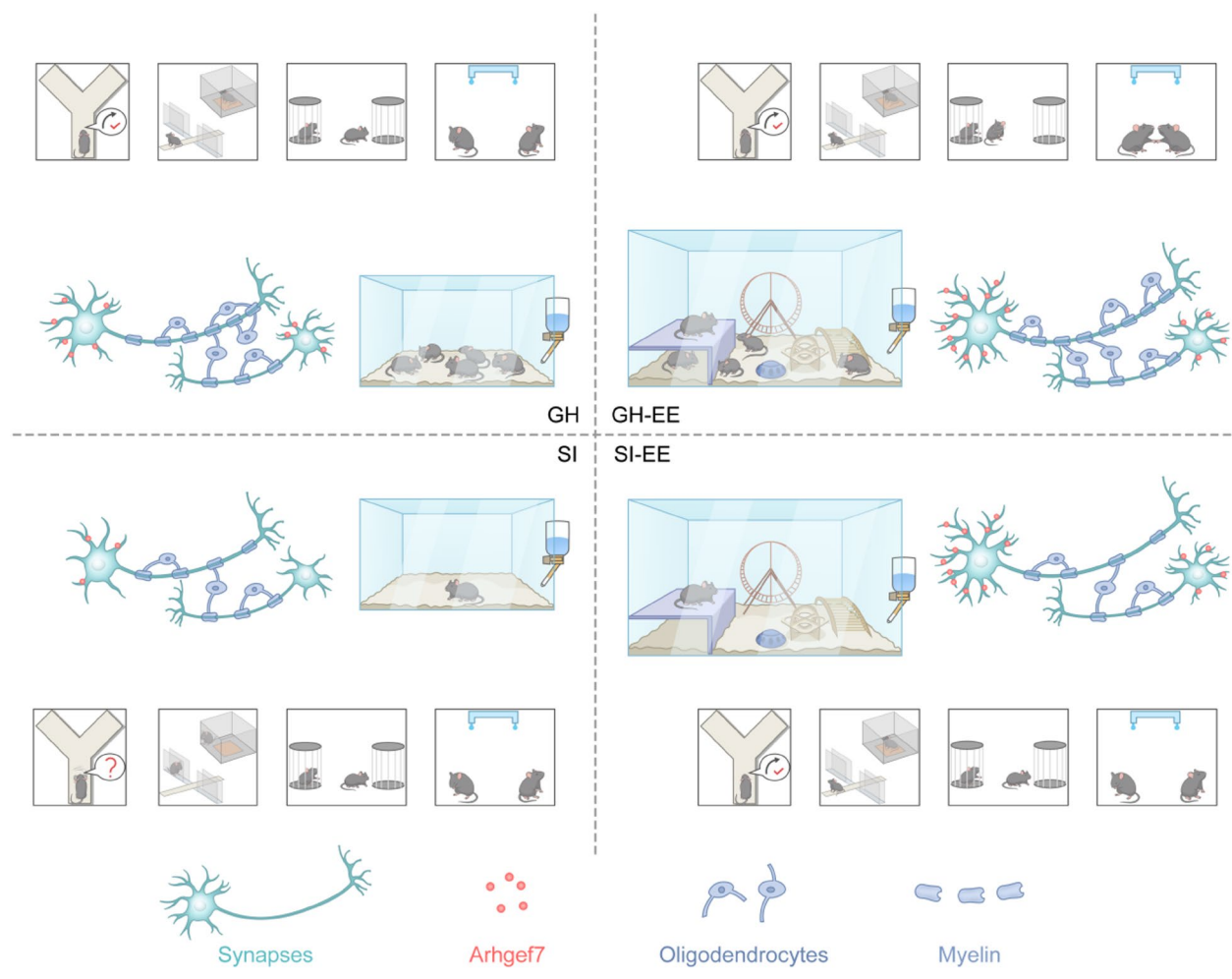
Yanli Zhang
yanlizhang0229@njmu.edu.cn
Junying Gao
gaojunying@njmu.edu.cn
Ming Xiao
mingx@njmu.edu.cn

Full list of author information is available at the end of the article



© The Author(s) 2025. **Open Access** This article is licensed under a Creative Commons Attribution-NonCommercial-NoDerivatives 4.0 International License, which permits any non-commercial use, sharing, distribution and reproduction in any medium or format, as long as you give appropriate credit to the original author(s) and the source, provide a link to the Creative Commons licence, and indicate if you modified the licensed material. You do not have permission under this licence to share adapted material derived from this article or parts of it. The images or other third party material in this article are included in the article's Creative Commons licence, unless indicated otherwise in a credit line to the material. If material is not included in the article's Creative Commons licence and your intended use is not permitted by statutory regulation or exceeds the permitted use, you will need to obtain permission directly from the copyright holder. To view a copy of this licence, visit <http://creativecommons.org/licenses/by-nc-nd/4.0/>.

Graphical abstract



Social isolation (SI) is defined as a state characterized by the absence of social interaction and support. It not only negatively impacts individuals' psychological and physiological health but may also lead to cognitive dysfunction, social avoidance behaviors, as well as mental disorders such as anxiety and depression [4]. An

increasing body of epidemiological evidence suggests that SI significantly increases the risk and accelerates the progression of AD [5]. Notably, adverse social stressors during early life exert profound and long-lasting negative impacts on cognitive abilities, social behaviors, and emotional regulation [6]. Exploring the mechanisms by which early-life stress influences the AD process and identifying potential interventions are crucial for the early prevention and treatment of AD.

Enriched environment (EE), as a safe and non-invasive intervention, can enhance cognitive function, emotional regulation, and neuroplasticity [7]. EE has been shown to promote neurogenesis and synaptic plasticity and reduce neuroinflammation and brain oxidative damage [8, 9], thereby delaying the progression of neurodegenerative diseases [10]. These benefits underscore the broad potential applications of EE. Previous studies have demonstrated that EE can ameliorate structural and functional impairments in the brain of rodents caused by SI [11, 12]. However, it must be emphasized that during animal experiments, EE consists of both physical and social components. The physical EE encompasses the expansion of housing space, the addition of toys, tunnels, running wheels, and alterations in the spatial arrangement of these items. Meanwhile, the enrichment of the social environment is typically achieved by increasing the number of animals housed in group settings [8–12]. Whether the physical components of EE alone can mitigate the exacerbating influence of SI on early AD, there is currently a lack of in-depth research, and its underlying mechanisms have not been fully elucidated.

The medial prefrontal cortex (mPFC) is a critical brain region for executive function, emotional regulation, cognitive control and social behavior [13]. It is particularly vulnerable in AD [14]. The mPFC is also one of the brain regions most significantly affected by both SI and EE [15, 16]. SI disrupts synaptic connectivity, dendritic spine, and myelin integrity in the mPFC [17]. In contrast, EE enhances synaptic plasticity and myelination, thereby mitigating the adverse effects of chronic stress on the developing forebrain [18]. These findings suggest that the mPFC may be involved in the course of SI and EE affecting AD pathology. However, the key regulatory molecules and their underlying mechanisms have not yet been fully elucidated.

Among the numerous factors involved in regulating synaptic structure and function, Rho guanine nucleotide exchange factor 7 (Arhgef7) has been identified as a critical regulator of dendritic spine morphogenesis and synaptic plasticity [19, 20]. Dysregulation of Arhgef7 is associated with various neuropsychiatric disorders such as schizophrenia [21, 22], autism spectrum disorder [23], and depression [24]. Yet its role in AD pathology remains largely unexplored.

In the current study, young adult 5×FAD transgenic mice were utilized to examine the effects and interactions of EE and early-life SI on cognitive function, anxiety-like phenotypes, and social and cooperative behaviors. The synaptic, myelinating glial cell activation, and β -amyloid (A β) deposition in the mPFC were compared among SI- or group-raised 5×FAD mice with or without the physical EE treatment. Through transcriptome sequencing and rescue experiments, Arhgef7 in mPFC neurons has been identified as the key target mediating the reversal effects of physical EE on cognitive deficits, dendritic atrophy, and synaptic degeneration in 5×FAD mice raised in isolation conditions. Our findings indicate that physical EE has beneficial effects on the restoration of cognitive and synaptic outcomes in previously isolated AD mice, but not on social behaviors or myelination.

Materials and methods

Animals and experimental design

5×FAD transgenic mice (carrying mutant human amyloid beta (A4) precursor protein 695 (APP) with the Swedish (K670N, M671L), Florida (I716V), and London (V717I) Familial Alzheimer's Disease (FAD) mutations along with human presenilin 1 (PS1) harboring two FAD mutations, M146L and L286V) were obtained from Jackson Laboratories. The mice were raised in the Experimental Animal Center of Nanjing Medical University. They were maintained in a controlled environment with a constant temperature (20–26 °C) and humidity (50–70%), under a 12-hour light/dark cycle, with free access to food and water.

5×FAD mice at 4 weeks of age were randomly divided into two groups: group-housed (GH) group, with five mice per cage, and SI group, with one mouse per cage. The mice were housed in standard cages (31 cm × 22 cm × 15 cm) for three weeks. Subsequently, the GH group was further randomly divided into two subgroups: the GH-control (GH-con) group, which maintained the original housing conditions, and the GH environmental enrichment (GH-EE) group, which was provided with an enriched physical environment. Similarly, the SI group was divided into the SI-control (SI-con) group, maintaining the original housing conditions, and the SI-EE group, which was also provided with an enriched physical environment. Both mice in the GH-EE and SI-EE groups were housed in larger plastic cages (47 cm × 30 cm × 23 cm) containing various objects such as running wheels, climbing ladders, and wooden huts to enhance sensory and motor stimulation. These objects were replaced every three to four days to maintain novelty. The experimental mice were continuously raised under the aforementioned conditions for 3 weeks, followed by a 2-week behavioral testing period, during which the original rearing conditions were maintained.

Furthermore, by conducting RNA sequencing and bioinformatics analysis on the mPFC of the aforementioned four groups of 5×FAD mice, we identified *Arhgef7* as a candidate gene that is significantly associated with cognitive function. To confirm that *Arhgef7* has the potential to enhance cognition and related pathologies under SI conditions, 1.5-month-old 5×FAD mice were randomly assigned to two groups: one group received bilateral mPFC injections of an adeno-associated virus 9 (AAV9) vector that overexpresses *Arhgef7* under the control of a neuron-specific hSyn promoter, while the other group served as the empty virus control group. After being raised under SI conditions for 3 weeks, we evaluated its regulatory effects on behavioral performance and pathological indicators. To further explore the regulatory effects of *Arhgef7* on cognitive function and AD-related pathologies, we selected 1.5-month-old 5×FAD mice and randomly divided them into two groups: one group received bilateral mPFC injections of an AAV9 vector expressing a short hairpin RNA (shRNA) targeting *Arhgef7* under the control of a neuron-specific hSyn promoter, and the other group served as the empty virus control group. Both groups of mice were raised under GH conditions for 3 weeks, followed by behavioral and neuropathological analyses.

Each group of mice consisted of an equal number of males and females. All animal experiments were conducted in compliance with the Guidelines for the Care and Use of Laboratory Animals of Nanjing Medical University (Ethical Approval Number: 1812054-4).

Behavioral tests

Open-field test

The open-field test was conducted to assess general locomotor activity, anxiety-like behavior, and exploratory willingness [25]. Individual mice were placed in an enclosed arena (60 cm × 60 cm × 25 cm) and allowed to move freely for 5 min. Their movements were recorded using an overhead camera to measure the total distance traveled, the time spent in the central area (30 cm × 30 cm), the number of entries into the central zone as well as the number of fecal boli and urine spots produced during the testing period.

Elevated plus maze test

The elevated plus maze (EPM) test, a widely used behavioral assay for assessing anxiety-like responses [26], consists of a central platform (10 cm × 10 cm), two elevated open arms (50 cm × 10 cm), and two enclosed arms (50 cm × 10 cm × 40 cm), elevated 100 cm above the ground. Mice were placed in the center of the apparatus and allowed to freely explore for 5 min. The number of entries into the open arms and the time spent in

the open arms were recorded to evaluate anxiety-related behaviors.

Y-maze test

The Y-maze test, conducted using a Y-shaped maze consisting of three arms (30 cm × 15 cm × 8 cm) with each arm angled at 120°, was employed to evaluate short-term working memory in mice [27]. The test consisted of two phases: a training phase and a testing phase, separated by an interval of 1 to 2 h. During the training phase, the novel arm was blocked with a partition, allowing the mice to freely explore the remaining two arms for 5 min. In the testing phase, the novel arm was unblocked, and the mice were permitted to freely explore all three arms for 5 min. The time spent in the novel arm and the numbers of entries into the novel arm were recorded using tracking software (TopScan, CleverSys, Inc., Reston, VA).

Three-chamber test

The three-chamber social test was conducted to evaluate social preference and social memory in mice. The experimental apparatus consisted of three equally sized rectangular chambers, each measuring 40 cm × 40 cm × 30 cm. Two adjacent chambers were separated by transparent polycarbonate walls featuring rectangular doorways (8 cm × 8 cm) to permit the mouse to move freely between the chambers. Two metal wire cages were placed in the outer chambers to house unfamiliar mice of the same sex, age, and coat color as the test mouse. The test was divided into three phases. In the first phase (habituation), the test mouse was allowed to explore all three chambers freely for 10 min. In the second phase (social preference test), an unfamiliar mouse (Stranger 1) was placed inside one of the metal-wire cages, and the test mouse was allowed to explore the chambers for 5 min. In the third phase, the social memory test, an unfamiliar second mouse (Stranger 2) was introduced into the opposite metal-wire cage, and the test mouse was permitted to explore the chambers for 5 min. The time the test mouse spent in each chamber during the social preference and social memory tests was recorded and analyzed to assess its social interaction and memory capabilities.

Social cooperation test

The cooperative drinking test was employed to evaluate the cooperative ability of mice [28]. The apparatus consisted of a polycarbonate cage (60 cm × 40 cm × 35 cm) equipped with two water dispensers and two light-sensitive switches that controlled the dispensers. Mice could obtain drinking water by activating the light-sensitive switches. The experiment was divided into two phases. In the initial phase (training phase), each mouse was placed in the apparatus following the activation of one of the light-sensitive switches. Over a 5-minute period,

the mouse was trained to explore and activate the other switch to access water. The training lasted for 7 days, with two sessions per day, alternating the active switch in each session. The latency to the first successful water access (drinking latency), the total time spent drinking (drinking time), and the number of water accesses (drinking number) were recorded during each training session. In the second phase (testing phase), both switches were deactivated, and two trained mice were placed in the apparatus together. Water was accessible only when both mice simultaneously activated their respective switches. Each pair was observed for 10 min, during which the latency to cooperative drinking (co-drinking latency), the total time spent drinking together (co-drinking time), and the number of cooperative drinking events (co-drinking number) were recorded. The testing phase lasted for 5 days, with one session per day. All mice were maintained in their original housing conditions, but were water-deprived for 8 h prior to each session.

Transcriptomic sequencing

Upon completion of the behavioral tests, the mice were euthanized, and their brain tissues were harvested. Total RNA was extracted from the mPFC tissues of GH-con, SI-con, GH-EE, and SI-EE mice using RNAiso Plus (Takara, #9109) as per the manufacturer's guidelines. The RNA's quality and quantity were evaluated using a NanoDrop 2000 (Thermo Scientific). RNA libraries were then constructed using the BGISEQ-500 platform, adhering to the manufacturer's protocol. Adapters were attached to both ends of the RNA molecules, followed by reverse transcription to produce single-stranded cDNA. Sequencing was conducted on the BGISEQ-500 platform, resulting in reads that were 50 base pairs (bps) in length. Subsequently, the mPFC sample datasets from the various groups were analyzed. The data from our study were deposited in the GEO repository, under the series record GSE283678.

Quantitative real-time PCR

Total RNA was extracted from the mPFC brain tissue samples of mice using Trizol (Takara, #9109). Following the manufacturer's instructions, 1 µg of total RNA was reverse-transcribed into cDNA using a reverse transcription kit (Takara, #RR047B). The cDNA was then amplified for 40 cycles using SYBR Green PCR master mix and detected on an ABI Step One Plus Real-Time PCR system (Applied Biosystems, Foster City, CA, USA). Relative quantification of target genes was performed using the $\Delta\Delta C_t$ method, with GAPDH serving as the internal reference.

Plasmids and adeno-associated viruses

The Arhgef7 overexpression plasmid was purchased from Tsingke Biotechnology Co., Ltd. (Nanjing, China). Arhgef7 siRNA and control siRNA were obtained from Ribobio Co., Ltd. (Guangzhou, China). Primary neurons were transfected with Arhgef7 siRNA, and the knock-down efficiency was assessed via Western blot 48 h post-transfection. The sequence of the mouse Arhgef7 siRNA was as follows: 5'-GAUCCUGAAGGUUAUCGAA-3', while the control siRNA sequence was: 5'-UUCGAUAA CCUUCAGGAUC-3'. The adeno-associated virus (AAV) for Arhgef7 knockdown, AAV-hSyn-Arhgef7-RNAi-EGFP(hSyn-siArhgef7-EGFP), and the AAV for Arhgef7 overexpression, AAV-hSyn-Arhgef7-EGFP, were purchased from GeneChem (Shanghai, China).

Stereotactic injection

Following anesthesia, the mice were secured in a stereotaxic apparatus. The cranial surface was disinfected, and the scalp was incised to expose the skull. Using a Hamilton syringe, 1.5 µL of AAV-hSyn-Arhgef7-RNAi-EGFP was bilaterally injected into the mPFC of GH-hSyn-siArhgef7-EGFP mice, while 1.5 µL of AAV-hSyn-Arhgef7-EGFP was administered to SI-hSyn-Arhgef7-EGFP mice within 10 min. The mPFC coordinates relative to bregma were: 1.6 mm anterior, ± 0.25 mm lateral, and 1.8 mm ventral. Five minutes after the injection, the needle was slowly withdrawn.

Primary neuron culture and cell transfection

Within 24 h after the birth of newborn mice, disinfection was performed using 75% ethanol, followed by rapid isolation of brain tissue. The isolated brain tissue was then placed in pre-cooled Dulbecco's Modified Eagle Medium (DMEM). The forebrain cortex was then dissected under a microscope using fine forceps. The tissues were sectioned and enzymatically digested in a DMEM solution containing 1 mg/ml DNase and 2 mg/mL papain, incubated at 37 °C for 15 min. Following digestion, the tissue suspension was transferred into a centrifuge tube. After centrifugation at 1000 *rpm* for 5 min, the pellet was resuspended in 2 mL of DMEM. A 200-mesh filter was used, and centrifugation was repeated at 1000 *rpm* for 5 min. The supernatant was discarded, and the pellet was resuspended in a pre-prepared neuronal culture medium. This medium consisted of Neurobasal-A supplemented with 2% B27, 1% antibiotics (penicillin and streptomycin), and 1% glutamine. The cells were then plated onto poly-D-lysine-coated wells and cultured in an incubator. The medium was refreshed every 3 days by replacing half of its total volume.

On the fifth day of primary neuronal culture, Arhgef7 siRNA and control siRNA were transfected into the cells using Lipofectamine 2000 (Invitrogen, USA),

following the manufacturer's instructions. Forty-eight hours post-transfection, the cell proteins were harvested. Concurrently, on the fifth day of the culture, the Arhgef7 overexpression plasmid was also transfected into the cells. After another 48 h, A β ₁₋₄₂ oligomers (Sigma, #T1892-25G; 10 μ M) were introduced and the cells were subjected to treatment for an additional 24 h. Following this treatment, the cell proteins were collected for analysis, and coverslips for immunofluorescence experiments were prepared.

Brain tissue preparation

After anesthetizing the mice with an intraperitoneal injection of ketamine, 0.1 M phosphate-buffered saline (PB) was perfused through the heart until the liver was blood-free. The brain tissue was then collected into an Eppendorf tube, quickly frozen in liquid nitrogen, and subsequently stored at -80 °C for protein immunoblotting experiments. For immunohistochemistry and immunofluorescence experiments, the brain was continuously perfused with 4% paraformaldehyde (PFA) for 5 min for fixation. The brain tissue was then stored in 4% PFA at 4 °C for 12 h. Some fixed brain samples were dehydrated using a gradient ethanol series, treated with xylene and embedded in paraffin. Sections with a thickness of 5 μ m were cut using a Leica paraffin slicer (Leica, Germany). The remaining brain samples were dehydrated in a gradient of 20% and 30% sucrose at 4 °C, followed by embedding in OCT compound. Sections of 20 μ m thickness were cut using a Leica slicer. For frozen sections, after washing with PBS, the tissue was mounted on slides, allowed to air dry, and then the subsequent steps were carried out promptly.

Thioflavin-S staining

Thioflavin-S is a standard fluorescent dye that specifically binds to amyloid protein deposits [29]. We utilized Thioflavin-S to detect A β plaques. Following deparaffinization and rehydration, the sections were stained with 0.1% Thioflavin-S (Nanjing Peptide Biotech Ltd.#107761-42-2) in the dark for 5 min, then washed under running water for 5 min and differentiated in 70% ethanol for another 5 min. Subsequently, the sections were mounted and observed under a fluorescence microscope for imaging.

Immunofluorescence

After deparaffinization and rehydration of the paraffin sections, antigen retrieval was performed using sodium citrate buffer via microwave heating for 15 min. For immunofluorescence staining, the brain sections or cell culture slides were blocked with blocking buffer (5% bovine serum albumin, 0.3% PBS-Triton X-100) for 1 h. The primary antibody (Table S1) was then applied and incubated overnight at 4 °C. Following a wash with

PBS, the corresponding secondary antibody was added and incubated for 2 h at room temperature in the dark. After washing with PBS, the sections were washed three times, with each wash lasting 10 min. The cell nuclei were stained with a 4,6-diamidino-2-phenylindole (DAPI) solution (diluted 1:1000 in PBS) for 10 min.

Golgi staining

According to the manufacturer's instructions (FD Rapid GolgiStain™ Kit (PK401), the fresh brain tissue was submerged in a solution combining Solution A and Solution B for 14 days, followed by a 24-hour incubation in Solution C. The tissue was subsequently sliced into 100 μ m thick sections using a cryostat and mounted onto glass slides. After air drying, the sections underwent dehydration in a sequence of ethanol solutions (50%, 75%, 95%, 100% I, and 100% II), were cleared with xylene, and mounted with neutral resin. Finally, the stained sections were examined under a microscope to observe the pyramidal neurons located in layers II/III of the mPFC.

Electron microscopy

Mice were anesthetized and perfused with 0.1 M PB to flush out the blood from the brain tissue. Subsequently, the brain was perfused with a 4% PFA solution for 7 min to fix the tissue. After the brain was removed, the mPFC region was dissected and fixed in 2.5% glutaraldehyde at 4 °C for a minimum of one week. Following the washing of the tissue, it was stained with 0.5% uranyl acetate and 75% ethanol for 1 h, followed by dehydration through a graded ethanol series and infiltration with propylene oxide. The tissue was then embedded in Epon and incubated at 60 °C for 24 h. The Epon blocks containing the mPFC tissue were trimmed and reoriented for sectioning. Thin sections with a thickness of 70 nm were cut using a Leica EM UC7 ultramicrotome. The samples were observed under a FEI Tecnai G2 electron microscope at an acceleration voltage of 120 kV (FEI, USA).

Image acquisition and quantitative analysis

The protocol for analyzing was as follows: Five mice were selected from each group, with at least one ultrathin section collected per mouse. Ten random fields of view were chosen from each section for investigation, resulting in a total analysis of 25 to 40 myelinated axons. Oligodendrocytes were identified based on their characteristic spindle-shaped morphology, the presence of microtubule structures, and the absence of intermediate filaments or glycogen granules. When calculating the *g*-ratio (i.e., the ratio of axon diameter to total fiber diameter), reference may be made to previous research literature. The threshold tool in ImageJ software (National Institutes of Health, USA) was used to select high-signal regions, thereby measuring the content of heterochromatin within the

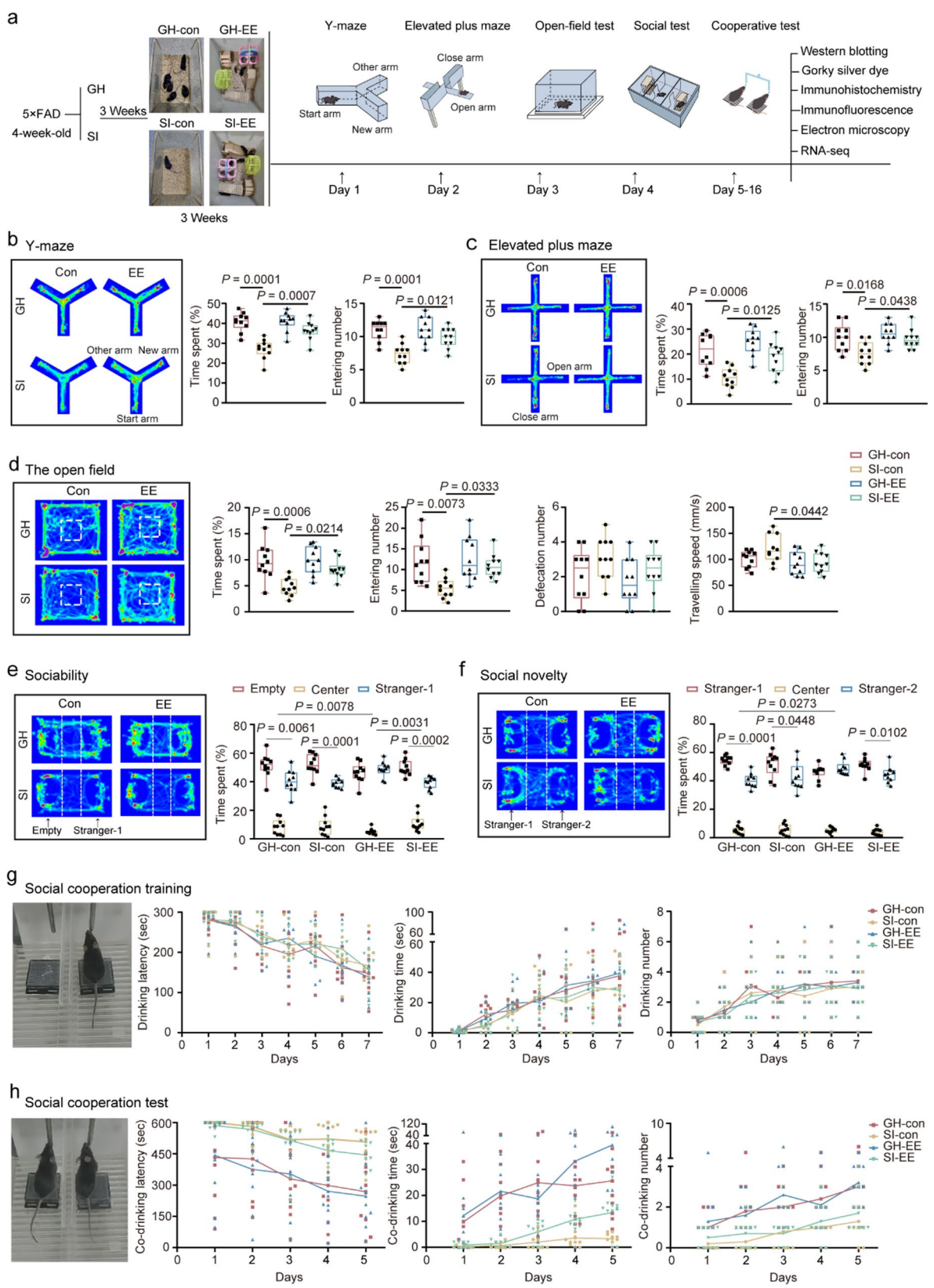


Fig. 1 (See legend on next page.)

(See figure on previous page.)

Fig. 1 5xFAD mice's behavior under different housing conditions. **A** Experimental design schematic. **B** The heat map of the mouse motion trajectory in the Y-maze test and the percentage of time spent in and the number of entering the new arm. **C** The heat map of the mouse movement in the elevated plus maze test and the percentage of time spent in and the number of entering the open arm. **D** The heat map of the mouse motion track in the open field test and the percentage of time spent in and the number of entering the central area, the amount of feces and the traveling speed during the test. **E** The heat map of the social preference test track of mice in the three-chamber test and the percentage of time the mice spent in each of the three chambers during the social preference test. **F** The heat map of the social memory test track of mice in the three-chamber test and the percentage of time spent in the three chambers during the social memory test. **G** The diagram of the training stage of the cooperative drinking water task and the time before the first drinking water (drinking latency), the total drinking time, and the number of drinking water during the training period. **H** The schematic diagram of the testing stage of cooperative drinking water task and the drinking latency, the total co-drinking time, and the number of co-drinking water during the testing period. $n = 10$ mice in each group (B–G), $n = 10$ pairs of mice in each group (H). Representative heatmaps showing mouse locomotor trajectories during the behavioral test. Color intensity indicates the frequency of occupancy in a given area, with darker colors representing more frequent visits. Significant differences were assessed using two-way ANOVA followed by Tukey's post hoc test. The within-group differences in the three-chamber social interaction test were assessed using unpaired Student's *t*-test. The data of cooperative drinking water were analyzed by repeated-measures ANOVA and post hoc Student-Newman-Keuls test

nucleus, expressed as a percentage of the total nuclear area. For evaluating synaptic ultrastructure, the width of the synaptic cleft was measured by uniformly selecting ten measurement points per synapse (delimited by the boundaries of the postsynaptic density). Synaptic curvature was calculated as the ratio of the arc length to the chord length of the presynaptic active zone.

The immunofluorescence micrographs were captured using a Zeiss LSM710 confocal microscope. Three non-repetitive coronal sections (spaced at least 100 μm apart) were selected from each mouse, with at least three randomly chosen fields analyzed per section. All microscopic images were processed using ImageJ software. For calculating the percentage of fluorescence-positive area (%), a uniform threshold was applied to all images to determine positive signals, followed by measurement of the target fluorophore area, which was expressed as a percentage of the total region of interest area. Positive cell counting was performed manually using ImageJ's "Cell Counter" plugin. Cells were considered positive when NeuN marker localization clearly showed nuclear or cytoplasmic staining. Finally, the counting results were normalized per square millimeter of tissue area.

The colocalization of fluorescent signals was also quantified using a line profile-based intensity analysis with ImageJ. For each representative merged image, the fluorescence channels were initially separated into individual single-channel images. Subsequently, a straight line or rectangular region of interest (ROI) was manually drawn along a fixed orientation (e.g., across a representative cell, process, or region with overlapping signals). The fluorescence intensity along the selected line or within the defined ROI was then measured separately for each channel using the "Plot Profile" function in ImageJ. The resulting intensity curves were exported and plotted to assess the spatial correlation between the two signals. Overlapping peaks in intensity profiles across channels were considered indicative of potential colocalization.

Western blot

The mPFC region was dissected on ice, homogenized in RIPA lysis buffer containing protease and phosphatase inhibitors, and lysed on an ice shaker for 30 min. Following centrifugation at 12,000 *rpm* for 15 min, the supernatant was collected, and the protein concentration was measured using a BCA assay. The protein lysate was subsequently mixed with loading buffer, heated at 95 $^{\circ}\text{C}$ for 5 min, and stored at -20°C .

For Western blot, 20–30 μg of protein samples were loaded onto a 10–15% SDS-polyacrylamide gel. The proteins were initially separated at 80 V for 35 min, followed by a run at 120 V for 60 min. After electrophoresis, the proteins were transferred onto a PVDF membrane using a constant current of 300 mA. Following the transfer, the membrane was blocked with 5% non-fat dry milk in TBST for 1 h. The membrane was then cut according to the molecular weight of the target protein, and the bands were incubated overnight at 4 $^{\circ}\text{C}$ with the primary antibody. The next day, the membrane was washed three times with TBST, for 10 min each time. It was then incubated with the appropriate HRP-conjugated secondary antibody at room temperature for 1 h. After thorough washing with TBST, protein bands were visualized using enhanced chemiluminescence reagents. GAPDH was used as the internal control for the protein.

Statistical analysis

Statistical analysis was performed using Prism 8.0 (GraphPad Software, USA). For comparisons between two groups, due to small sample sizes ($n = 6$ or 10 per group), we verified data distribution visually at first and performed both parametric (*t*-test) and non-parametric (Mann–Whitney *U* test) comparisons to ensure statistical robustness. For comparisons involving three or more groups, one-way or two-way ANOVA was applied, followed by Tukey's post hoc test for multiple comparisons. Social cooperation test data were analyzed using repeated-measures ANOVA. Data are presented as mean \pm SEM. Statistical significance was set at $P < 0.05$.

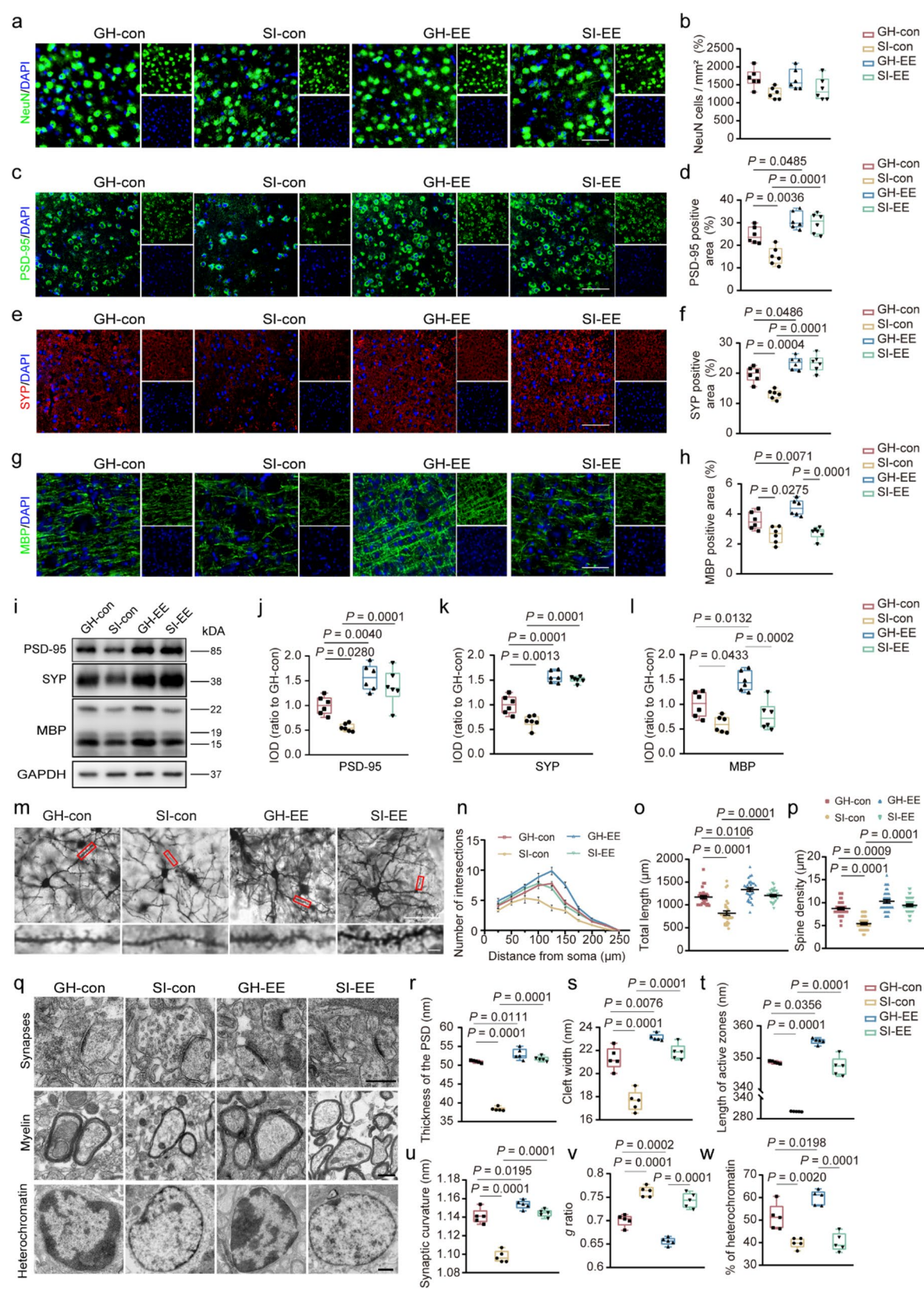


Fig. 2 (See legend on next page.)

(See figure on previous page.)

Fig. 2 Pathology of synapses, spines, and myelin in the mPFC of 5×FAD mice under various housing conditions. **A–H** Representative images of immunofluorescence for NeuN (A), PSD-95 (C), SYP (E), MBP (G) of the four groups. Scale bar: 50 μ m. And the number of NeuN positive neurons per unit area (B), quantitative analysis of the PSD-95 positive area (D), SYP positive area (F), MBP positive area (H), ($n=6$). **I** Representative Western blot bands of PSD-95, SYP, and MBP of the four groups. **J–L** The gray values of bands for PSD-95 (J), SYP (K), and MBP (L), ($n=6$). **M** Golgi staining of the four groups. Scale bar: neurite 50 μ m, dendritic spine 2 μ m. **N** The distribution of dendrite length with distance from the cell body. Each group consists of 6 mice, with 5 neurons counted for each mouse. **O** The total length of neurites of the four groups. **P** Density of dendritic spines. The data came from six mice in each group, each with six dendritic spines. **Q** Representative EM images showing synaptic morphology (top), myelin sheath (middle), and OLs nuclear heterochromatin (bottom) of the four groups. Scale bar, 500 nm. **R–U** Quantification of PSD, synaptic cleft width, active zone length, and synaptic curvature in GH-con (76 synapses), SI-con (80 synapses), GH-EE (74 synapses) and SI-EE (78 synapses) groups. $n=5$ mice per group. **V** The scatterplot of myelin g-ratio in GH-con (122 axons), SI-con (122 axons), GH-EE (111 axons) and SI-EE (117 axons) groups. **W** The area percentage of OLs nuclear heterochromatin in region of the four groups. GH-con (16 nuclei), SI-con (19 nuclei), GH-EE (15 nuclei), and SI-EE (17 nuclei). $n=5$ mice per group. Significant differences were assessed using two-way ANOVA followed by Tukey's post hoc test

Results

Heterogeneous beneficial effects of physical EE on behavioral outcomes in early isolated 5×FAD mice

Behavioral and histopathological analyses were conducted on 5×FAD mice within the GH group, SI group, GH-EE group, and SI-EE group to investigate the effects of physical EE and early SI on AD-like pathophysiology (Fig. 1A). The short-term spatial memory was assessed using the Y-maze test. The results indicated that, compared to GH-5×FAD mice, SI-5×FAD mice exhibited a significant decrease in both the time spent in the novel arm and the number of entries into the novel arm. Conversely, physical EE resulted in a notable enhancement in both the time spent in the novel arm and the number of entries into the novel arm for GH-EE and SI-EE groups (Fig. 1B). Additionally, we evaluated anxiety-like behaviors in mice using the EPM and open-field tests. SI-5×FAD mice exhibited a significant decrease in the percentage of time spent on the open arms and a reduced number of entries into these arms of the EPM, compared with GH-5×FAD controls. Conversely, SI-5×FAD mice raised under the physical EE demonstrated an increased percentage of time on the open arms and a higher number of entries into them. (Fig. 1C). SI-5×FAD mice displayed a significant decline in exploratory behavior in the open-field test, evidenced by less time spent in the center zone and fewer entries into this zone. SI-5×FAD mice raised in the physical EE effectively alleviated the exploratory deficits (Fig. 1D). Interestingly, the aforementioned short-term memory or anxiety-like phenotypes were not different between GH-5×FAD mice and GH-EE-5×FAD mice.

We also employed the three-chamber test to examine the impact of the physical EE on social interaction in 5×FAD mice subjected to early-life SI. SI-5×FAD mice demonstrated deficits in both social interaction and preference for social novelty, whereas the physical EE did not alleviate these social impairments. Intriguingly, GH-EE-5×FAD mice exhibited better social behavior performance compared to GH-5×FAD mice (Fig. 1E, F). Subsequently, we employed a cooperative drinking behavioral paradigm, previously established by our

laboratory [28], to further evaluate the social cooperative abilities of these mice. The training phase results indicated that 5×FAD mice from all groups successfully learned and mastered the cooperative drinking task, with no significant differences in drinking latency, total drinking duration, or the number of drinking bouts (Fig. 1G). During the testing phase, compared to GH-5×FAD controls, SI-5×FAD mice exhibited increased drinking latency and decreased drinking duration and number. However, the physical EE did not significantly improve the cooperative abilities compromised by SI. Compared to GH-5×FAD mice, GH-EE-5×FAD mice showed a significant reduction in drinking latency, along with a marked increase in both the number of drinking bouts and total drinking time (Fig. 1H). Collectively, these findings demonstrate that 3.5-month-old 5×FAD mice that previously subjected to SI exhibit significant impairments in spatial cognitive, social interaction and cooperative abilities and anxiety-like behaviors. The physical EE selectively alleviates SI-induced spatial cognitive deficits and anxiety-like behavior.

Physical EE alleviated neuronal degeneration in the mPFC of SI-5×FAD mice, but failed to mitigate hypomyelination

Both 6E10 immunofluorescence and Thioflavin-S staining demonstrated that SI increased A β plaque deposition in the mPFC of 5×FAD mice. Whereas GH-5×FAD mice, rather than SI-5×FAD mice, housed in the physical EE showed reductions in A β plaque burden (Figure S1A–C). Compared to GH-5×FAD controls, SI-5×FAD mice displayed increased proportional areas of glial fibrillary acidic protein (GFAP) positive astrocytes and ionized calcium binding adaptor molecule-1 (Iba1) positive microglia in the mPFC. Notably, the physical EE intervention reduced activation of astrocytes and microglia in both SI- and GH-5×FAD mice (Figure S1D–G).

We further analyzed the effects of SI and/or physical EE on neuronal number, dendritic morphology, and synaptic integrity in the mPFC of 5×FAD mice. No significant differences in the number of NeuN-positive neurons in the mPFC were observed among the four groups (Fig. 2A, B). However, immunofluorescence and Western

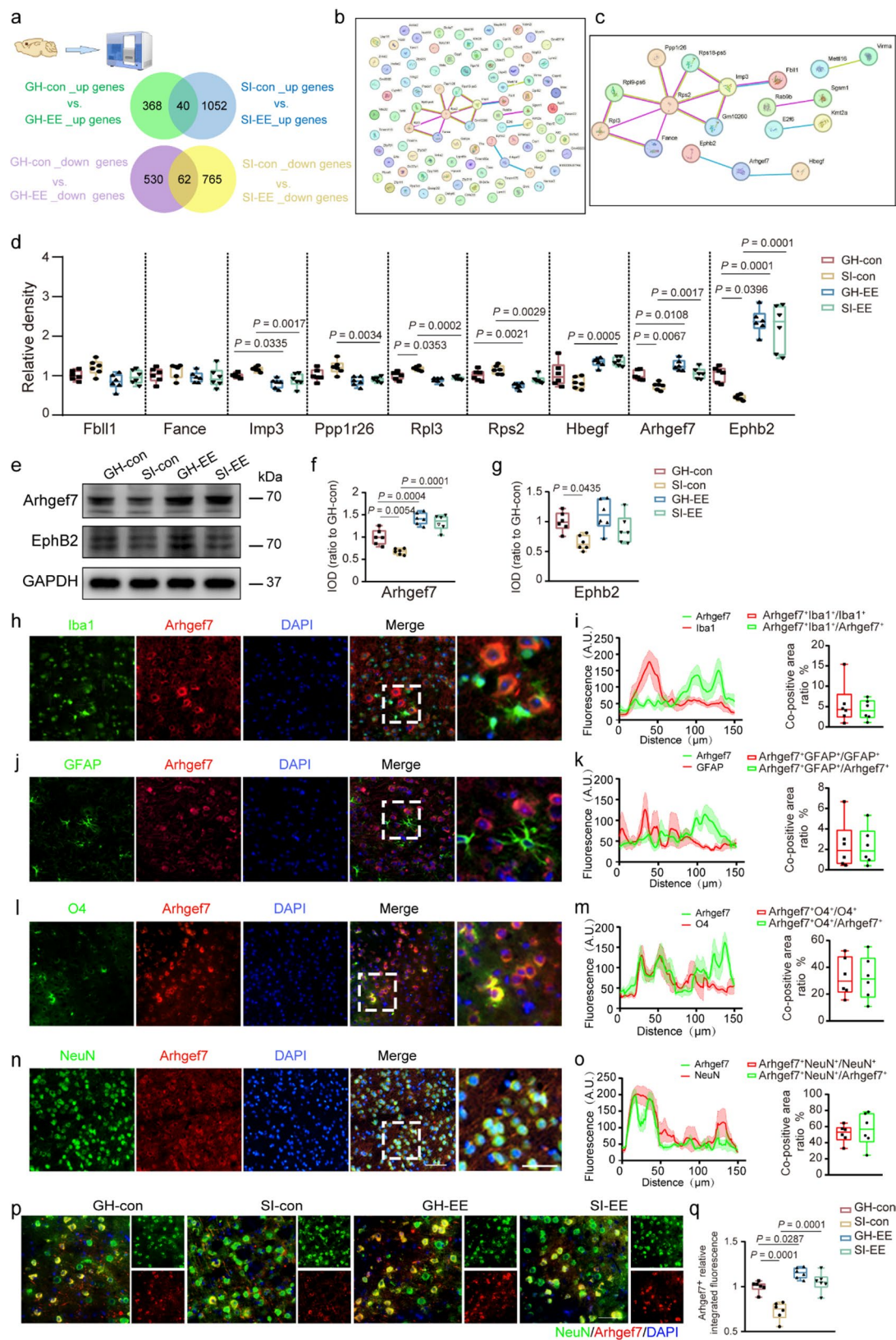


Fig. 3 (See legend on next page.)

(See figure on previous page.)

Fig. 3 Screening and identification of potential genes for EE improving cognitive function in 5×FAD mice. **A** Venn diagram showing the overlap analysis of differentially expressed genes (DEGs) between the GH and SI groups after EE treatment, with 40 upregulated genes and 62 downregulated genes. **B** Protein-protein interaction (PPI) network of the DEGs. **C** Gene clusters selected from the screening. **D** The qPCR validation of the transcriptional level changes of the selected genes in the mPFC of the four groups ($n=6$). **E** Western blot of Arhgef7 and EphB2 in the mPFC of each group. **F–G** Statistical analysis of gray values of bands for Arhgef7 (F) and EphB2 (G) ($n=6$). **H** Immunofluorescence images showing co-localization of Arhgef7 with Iba1-positive microglia. **I** Left: Volcano plot showing co-localization of Arhgef7 with Iba1 (H); Right: Percentage of co-localization area between Arhgef7 and Iba1. **J** Immunofluorescence images showing co-localization of Arhgef7 with GFAP-positive astrocytes. **K** Left: Volcano plot showing co-localization of Arhgef7 with GFAP (J); Right: Percentage of co-localization area between Arhgef7 and GFAP. **L** Immunofluorescence images showing co-localization of Arhgef7 with O4-positive oligodendrocytes. **M** Left: Volcano plot showing co-localization of Arhgef7 with O4 (L); Right: Percentage of co-localization area between Arhgef7 and O4. **N** Immunofluorescence images showing co-localization of Arhgef7 with NeuN-positive neurons. Left: Scale bar bar: 50 μm ; Right: Scale bar: 20 μm . **O** Left: Volcano plot showing co-localization of Arhgef7 with NeuN (N); Right: Percentage of co-localization area between Arhgef7 and NeuN. **P** Immunofluorescence images of NeuN and Arhgef7 in the mPFC of the four groups. Scale bar: 50 μm . **Q** The relative integrated fluorescence signal of Arhgef7-positive area in the mPFC of each group ($n=6$). Significance differences were assessed using two-way ANOVA followed by Tukey's post hoc test (D, F, G, Q) or two-tailed Student's t-test (I, K, M, O)

blot analyses consistently demonstrated that SI significantly reduced the expression levels of synaptic proteins, including postsynaptic density protein-95 (PSD-95) and synaptophysin (SYP), in the mPFC. These alterations were effectively rescued by the physical EE (Fig. 2C–F, I–K). Golgi staining also revealed that, compared to the GH group, the SI group exhibited significantly reduced neurite complexity and dendritic spine density. The physical EE markedly improved dendritic plasticity in both the GH and SI groups (Fig. 2M–P). The EM and quantitative analyses further revealed that SI impaired the ultrastructural integrity of synapses in the mPFC of 5×FAD mice, as evidenced by reductions in postsynaptic density, synaptic cleft width, active zone length, and synaptic curvature. Notably, the physical EE restored these ultrastructural alterations in SI-5×FAD mice and further enhanced synaptic parameters in GH-5×FAD mice (Fig. 2Q–U).

To evaluate the myelination status in the mPFC, we conducted immunofluorescence and Western blot analyses for myelin basic protein (MBP) across the experimental groups. The findings indicated that SI resulted in hypomyelination in the mPFC of 5×FAD mice, evidenced by diminished MBP immunopositive intensity. Notably, the physical EE enhanced myelination in GH-5×FAD mice but did not rescue the hypomyelination phenotype in SI-5×FAD mice (Fig. 2G–I, L). The EM and quantitative analyses confirmed the detrimental effect of SI on myelination in 5×FAD mice, as evidenced by an elevated g -ratio and a reduction in heterochromatin within oligodendrocytes. The physical EE improved myelination in GH-5×FAD mice, but not in SI-5×FAD mice (Fig. 2Q, W).

Physical EE restored downregulated Arhgef7 expression in mPFC neurons of SI-5×FAD mice

To investigate the molecular mechanisms underlying the ameliorative effects of the physical EE on behavioral abnormalities in 5×FAD mice, RNA sequencing (RNA-seq) was performed on mPFC tissue samples from the four groups (Fig. 3A). Differential gene expression analysis was performed between GH-con and GH-EE groups,

as well as between SI-con and SI-EE groups. Comparative analysis revealed 408 upregulated and 592 downregulated genes in GH-con group vs. GH-EE group, and 1,092 upregulated and 827 downregulated genes in SI-con group vs. SI-EE group. Subsequently, the intersection of upregulated and downregulated genes from both comparisons was identified, yielding 102 differentially expressed genes, including 40 upregulated and 62 downregulated genes (Fig. 3B). Protein-protein interaction (PPI) network analysis was subsequently applied to prioritize gene clusters with robust functional relevance and literature support (Fig. 3C), such as *Fbll1*, *Fance*, *Imp3*, *Ppp1r26*, *Rpl3*, *Rps2*, *Hbegf*, *Arhgef7*, and *Ephb2*.

To validate these findings, quantitative real-time PCR (qPCR) was performed on mPFC tissues from all four experimental groups. The results revealed that the physical EE downregulated *Imp3* and *Rps2* while upregulating *Arhgef7* and *Ephb2* both in GH and SI groups. Additionally, the transcription levels of *Ppp1r26* and *Rpl3* were downregulated, and *Hbegf* was upregulated, but this was observed only in the SI group. Intriguingly, compared to GH-5×FAD mice, SI-5×FAD mice also showed downregulated the transcription levels of *Arhgef7*, *Ephb2*, and *Rpl3* (Fig. 3D). Among these genes, *Imp3* and *Rps2* are primarily implicated in RNA transport, translation, and ribosome biogenesis [30, 31]. In contrast, *Arhgef7* and *Ephb2* are predominantly localized to synapses, where they regulate synaptic function and dendritic spine morphogenesis [32–34]. Western blot analysis further demonstrated that Arhgef7 protein levels were markedly reduced in SI-5×FAD mice but restored by the physical EE (Fig. 3E–G). To ascertain the cellular localization of Arhgef7, double immunofluorescence staining was conducted using markers for microglia (Iba1), astrocytes (GFAP), oligodendrocytes (O4), and neurons (NeuN, a neuronal nuclear antigen), in conjunction with Arhgef7. The results indicated that Arhgef7 was predominantly expressed in mPFC neurons (Fig. 3H–O), aligning with previous reports [35]. Additionally, analysis of cumulative fluorescence intensity demonstrated that SI decreased Arhgef7 expression in mPFC neurons of 5×FAD mice,

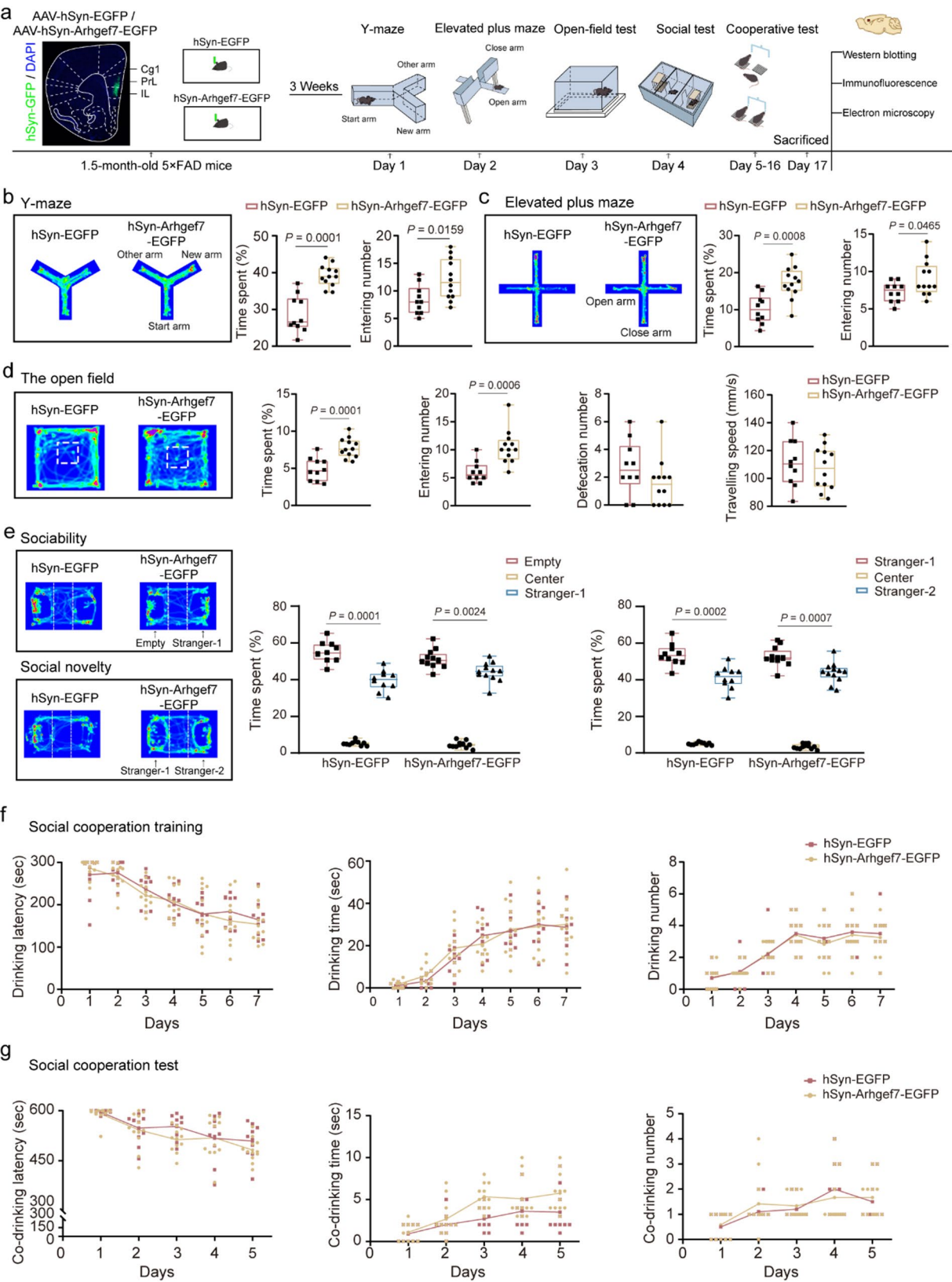


Fig. 4 (See legend on next page.)

(See figure on previous page.)

Fig. 4 Arhgef7 overexpression alleviated cognitive deficits and anxiety-like behavior but did not improve social impairments in the SI group. **A** Experimental design schematic. **B** Left: the heatmap showing the movement trajectory of 5×FAD mice in SI-hSyn-EGFP group and SI-hSyn-Arhgef7-EGFP group in the Y-maze test; Right: the percentage of time spent in and number of entries into the novel arm. **C** Left: the heatmap of mouse movement trajectories in the elevated plus maze test; Right: the percentage of time spent in and number of entries into the open arms. **D** Left: the heatmap of mouse movement trajectories in the open field test; Right: the percentage of time spent in the center area, number of entries into the center, fecal count, and travel speed. **E** Left: the heatmap of mouse trajectories during social preference and social memory tests in the three-chamber test; Right: the percentage of time spent in each chamber during the social preference and social memory tests. **F** The graphs showing latency to first drink, total drinking time, and number of drinking events during the training stage of the social cooperation test. **G** The graphs showing latency to first drink, total co-drinking time, and number of co-drinking events during the test stage of the social cooperation test. SI-hSyn-EGFP group, $n = 10$; SI-hSyn-Arhgef7-EGFP group, $n = 12$ in (B-E). SI-hSyn-EGFP, $n = 10$ pairs; hSyn-Arhgef7-RNAi-EGFP group, $n = 12$ pairs in (G). Significant differences were assessed using two-tailed Student's *t*-tests. The data of cooperative drinking water test were analyzed by repeated-measures ANOVA and post hoc Student-Newman-Keuls test

whereas EE elevated Arhgef7 expression in both GH- and SI-5×FAD mice (Fig. 3P, Q).

Arhgef7 overexpression in mPFC neurons rescued spatial cognitive dysfunction and anxiety-like behavior in SI-5×FAD mice without affecting social behavior

To clarify the role of Arhgef7 in early SI-induced behavioral and structural alterations, 1.5-month-old 5×FAD mice were administered bilateral injections of an AAV9 vector that specifically overexpresses Arhgef7 in neurons into the bilateral mPFC. The mice were then individually raised for 3 weeks, followed by a series of behavioral tests and pathological analyses (Fig. 4A; Figure S2A-C). Y-maze testing revealed that compared to SI-hSyn-EGFP controls, SI-hSyn-Arhgef7-EGFP mice showed enhanced short-term memory, as evidenced by a greater duration spent in the novel arm and a higher frequency of entries into the novel arm (Fig. 4B). Furthermore, during the EPM and open field tests, SI-hSyn-Arhgef7-EGFP mice exhibited increased percentages of time spent in the open arms and a greater number of entries into these arms (Fig. 4C), as well as extended time spent and more frequent entries into the center zone (Fig. 4D), suggesting a reduction in anxiety-like behaviors. However, the three-chamber test and social cooperation test demonstrated that overexpression of Arhgef7 did not alleviate social interaction deficits or cooperative abilities in SI mice (Fig. 4E-G).

Arhgef7 overexpression in mPFC neurons improved dendritic and synaptic integrity, but not myelin, in SI-5×FAD mice

Consistent with behavioral outcomes, overexpression of Arhgef7 did not impact the quantity of NeuN-positive neurons (Fig. 5A-B). However, it improved dendritic and synaptic structural parameters in SI-5×FAD mice, such as the fluorescence-positive area and protein expression levels of PSD-95 and SYP, axonal complexity, dendritic spine density, postsynaptic density, and synaptic curvature (Fig. 5C-F, I-K, M-U). Nevertheless, Arhgef7 overexpression in SI-5×FAD mice did not significantly affect oligodendrocyte morphology, myelin *g*-ratio, heterochromatin levels, or MBP expression (Fig. 5G-I, L,

V-Y). Additionally, Arhgef7 overexpression did not alter Aβ plaque deposition or the activation of microglia and astrocytes in the mPFC of SI-5×FAD mice (Figure S2D-K).

Arhgef7 knockdown in mPFC neurons caused spatial cognitive dysfunction and anxiety-like behavior in 5×FAD mice without affecting social behavior

Previous studies have shown that Arhgef7 promotes neurite outgrowth in primary cortical neurons [36], and its conditional knockout in dorsal root ganglia diminishes neurite elongation [37]. To further ascertain the necessity of Arhgef7 for sustaining neuronal processes integrity during the early stages of 5×FAD mice, we engineered an AAV9 vector encoding a short hairpin RNA (shRNA) against Arhgef7, regulated by a neuron-specific hSyn promoter, and incorporating a separate GFP expression cassette. The siArhgef7 virus was bilaterally injected into the mPFC of 1.5-month-old 5×FAD mice. Subsequently, the mice underwent group housing for three weeks, followed by behavioral tests and pathological analyses (Fig. 6A). GFP fluorescence was clearly observed in mPFC neurons, indicating successful viral transduction (Figure S3A). Western blot analysis also confirmed the effectiveness of Arhgef7 knockdown (Figure S3B-C).

The Y-maze test revealed that hSyn-siArhgef7-EGFP-5×FAD mice exhibited impaired short-term memory compared to hSyn-EGFP-5×FAD controls, as evidenced by reduced time spent in the novel arm and fewer entries into the novel arm (Fig. 6B). Similarly, Arhgef7 knockdown also decreased the percentage of time spent in the open arms of the elevated plus maze and reduced entries into the open arms (Fig. 6C), along with decreased time and entries into the center zone of the open field (Fig. 6D). However, the three-chamber test and social cooperation test demonstrated that Arhgef7 knockdown did not exacerbate deficits in social memory, social preference, or cooperative abilities in 5×FAD mice (Fig. 6E-G).

Arhgef7 knockdown exacerbated dendritic and synaptic, but not myelin, damage in the mPFC of GH-5×FAD mice

Histopathological analysis was conducted to explore whether there was heterogeneity in the protective effect of the Arhgef7 gene on neurons and oligodendrocytes during the progression of AD. Knockdown of Arhgef7 did not alter the number of NeuN-positive neurons (Fig. 7A–B), but it significantly reduced the fluorescence-positive area and the protein expression levels of PSD-95, SYP, and MBP (Fig. 7C–F, I–K). Furthermore, Arhgef7 knockdown markedly decreased axonal complexity and dendritic spine density (Fig. 7M–P). The EM revealed reductions in postsynaptic density, synaptic cleft width, active zone length, and synaptic curvature in the mPFC of hSyn-siArhgef7-EGFP mice (Fig. 7Q–U). However, no significant differences were observed in MBP expression, myelin g-ratio, or heterochromatin levels of oligodendrocyte nuclei between the hSyn-siArhgef7-EGFP and hSyn-EGFP groups (Fig. 7G–I, L, V–Y). These findings suggest that Arhgef7 knockdown selectively impairs neuronal processes and synaptic integrity without significantly affecting myelination.

We further assessed A β plaque deposition and glial activation in the mPFC of 5×FAD mice, with or without Arhgef7 knockdown. No significant increase in A β plaque burden was observed in the hSyn-siArhgef7-EGFP group compared to the control group (Figure S3D–G). Additionally, Arhgef7 knockdown did not significantly alter the activation levels of microglia or astrocytes, as quantified by Iba1 and GFAP immunofluorescence intensities, respectively (Figure S3H–K).

Arhgef7 protected cortical neurons against A β toxicity through Wnt signaling

To validate the functional role of Arhgef7 in cortical neurons, we transfected primary cortical neurons with Arhgef7 siRNA, achieving efficient knockdown (Fig. 8A, B). Neurons with Arhgef7 knockdown exhibited significantly reduced axonal length and branching (Fig. 8C–E). We also treated cortical neurons with A β_{1-42} oligomers (10 μ M) to investigate whether Arhgef7 mitigates A β -induced neuronal toxicity. Overexpression of Arhgef7 via plasmid transfection markedly enhanced neurite outgrowth and rescued A β_{1-42} -induced neuronal degeneration (Fig. 8F–H). These findings underscore the critical role of Arhgef7 in promoting neurite growth and protecting neurons against A β toxicity. A β deposition is strongly associated with synaptic dysfunction in AD [38]. Multiple signaling pathways, including Hippo, MAPK, NMDA, PI3K/AKT, and Wnt/ β -catenin, have been implicated in synaptic regulation during AD pathogenesis [39–43]. To explore the molecular mechanisms underlying Arhgef7's resistance to A β neurotoxicity and the enhancement of synaptic function, we analyzed pathway alterations in vitro and

in vivo through Western blot assays. A β_{1-42} treatment increased the phosphorylation of MST1, ERK1/2, NR2B, and β -catenin, while decreasing the phosphorylated levels of PI3K and AKT in primary cortical neurons. In contrast, the overexpression plasmid of Arhgef7 markedly activated the Wnt- β -catenin and PI3K-AKT signaling pathways in primary cortical neurons, counteracting the inhibitory effects on these pathways induced by A β treatment (Fig. 8I, J, S4A). Additionally, the critical regulatory role of Arhgef7 in the Wnt/ β -catenin signaling pathway and the PI3K/AKT signaling pathway was further confirmed in primary cortical neurons treated with Arhgef7 siRNA (Fig. 8K, L, S4B). In the mPFC of SI-5×FAD mice, the phosphorylation level of β -catenin was significantly increased, whereas the levels of p-PI3K and p-AKT were markedly decreased, indicating suppression of both the Wnt/ β -catenin and PI3K/AKT signaling pathways. Conversely, the physical EE significantly activated these pathways in both GH and SI groups (Fig. 8M, N, S4C). Furthermore, overexpression of Arhgef7 in mPFC neurons of SI-5×FAD mice significantly suppressed β -catenin phosphorylation and enhanced PI3K/AKT phosphorylation (Fig. 8O, P, S4D). Conversely, in GH-5×FAD mice, knockdown of Arhgef7 increased β -catenin phosphorylation but did not significantly inhibit PI3K/AKT signaling (Fig. 8Q, R, S4E). In summary, these data suggest that Arhgef7 may primarily alleviate A β -induced synaptic damage in the cortex by activating the Wnt/ β -catenin signaling pathway, thereby improving cognitive dysfunction in AD and delaying the pathological progression of the disease.

Discussion

AD remains an unresolved major medical challenge in modern society, with its pathogenesis not fully understood [44]. Current research indicates that the onset of AD is associated with multiple factors, including genetics, aging, environmental influences, and social behaviors [44, 45]. As a detrimental environmental factor, SI has been identified as a strong risk factor for AD progression [46]. Conversely, healthy lifestyles have shown significant benefits in AD prevention and intervention [47]. This study investigated the ameliorating effects of physical components of EE on SI-induced behavioral and pathological alterations in the early stage of 5×FAD mice.

Negative social experiences during childhood, such as social abuse and neglect, have profound effects that persist into adulthood. Synapse development is completed in three-week-old mice, while myelination in the central nervous system occurs later and lasts until the end of adolescence [48]. 5×FAD mice are a transgenic model widely used in AD research. A β plaques began to be deposited in the cortex of 5×FAD mice at 1.5 months of age; at 2 months of age, obvious activation of glial

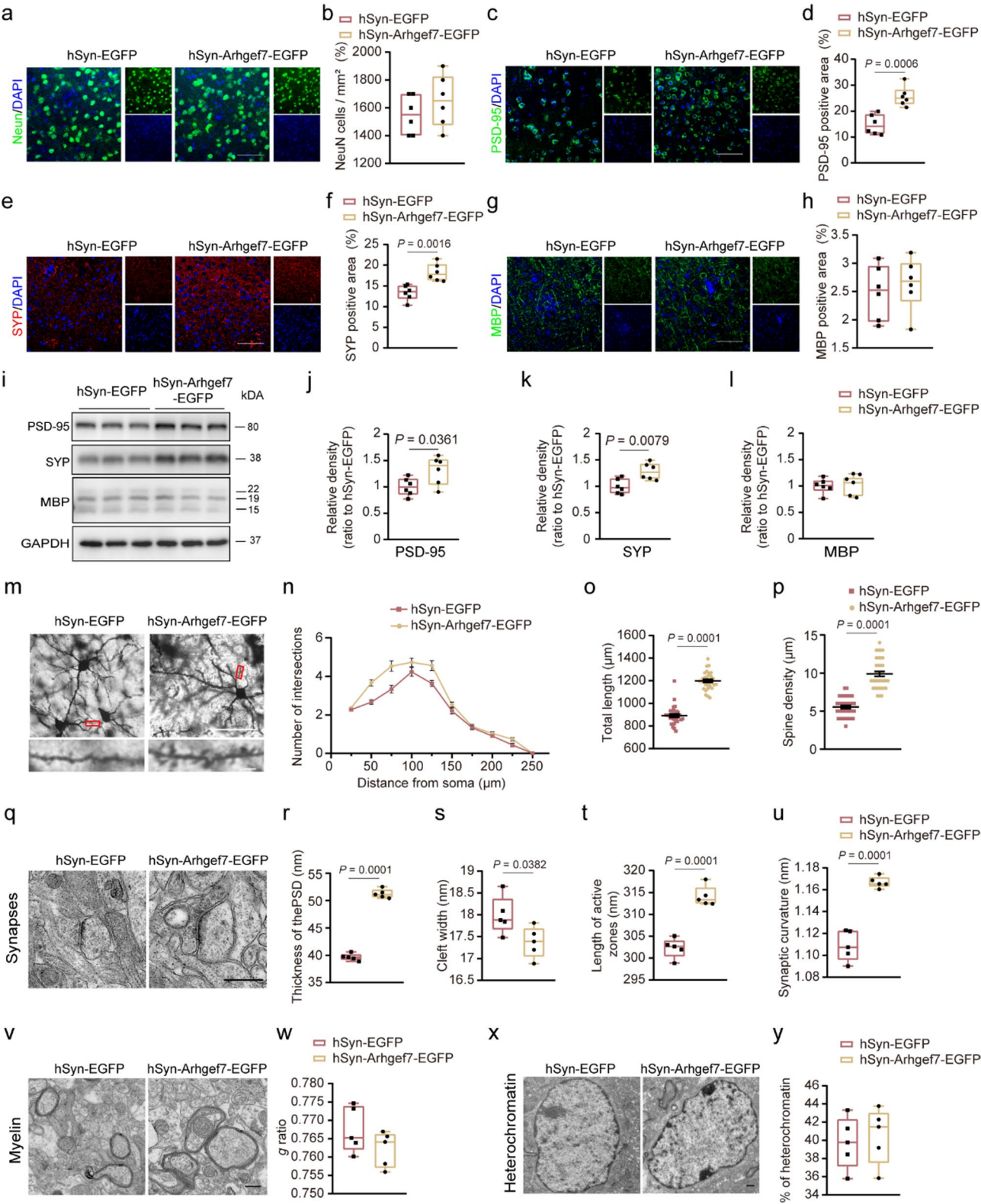


Fig. 5 (See legend on next page.)

(See figure on previous page.)

Fig. 5 Arhgef7 overexpression prevented dendritic and synaptic impairments but failed to preserve myelin sheath integrity in the mPFC of SI groups. **A–H** Representative images of immunofluorescence for NeuN (A), PSD-95 (C), SYP (E), MBP (G) of 5×FAD mice in SI-hSyn-EGFP group and SI-hSyn-Arhgef7-EGFP group. Scale bar: 50 μ m. And the number of NeuN positive neurons per unit area (B), quantitative analysis of the PSD-95 positive area (D), SYP positive area (F), MBP positive area (H), ($n=6$). **I** Representative Western blot bands of PSD-95, SYP, and MBP of the two groups. **J–L** The gray values of bands for PSD-95 (J), SYP (K), and MBP (L) ($n=6$). **M** Golgi staining of the two groups. Scale bar: neurite 50 μ m, dendritic spine 2 μ m. **N** The distribution of dendrite length with distance from the cell body. Each group consists of 6 mice, with 5 neurons counted for each mouse. **O** The total length of neurites of the two groups. **P** Density of dendritic spines. The data came from six mice in each group, each with six dendritic spines. **Q** Representative EM images showing synaptic morphology of 5×FAD mice in the two groups. Scale bar, 500 nm. **R–U** Quantification of PSD, synaptic cleft width, active zone length, and synaptic curvature in SI-hSyn-EGFP group and SI-hSyn-Arhgef7-EGFP group. 75 synapses per mouse, $n=5$ mice per group. **V** Representative EM images showing myelin sheath of 5×FAD mice in the two groups. Scale bar, 500 nm. **W** The scatterplot of myelin g-ratio in SI-hSyn-EGFP group (110 axons) and SI-hSyn-Arhgef7-EGFP group (112 axons) ($n=5$). **X** Representative EM images showing OLs nuclear heterochromatin of 5×FAD mice in the two groups. Scale bar, 500 nm. **Y** The area percentage of OLs nuclear heterochromatin of 5×FAD mice in the two groups. 25 synapses per mouse, $n=5$ mice per group. Significant differences were assessed using two-tailed Student's *t*-tests

cells was observed; at 3 months of age, the mice gradually exhibited a decline in social behavior and emotional disorders; and at 4 months of age, a significant decline in cognitive function began to manifest [49–51]. Consequently, this study selected 4-week-old 5×FAD mice for a 3-week period of SI, followed by a 3-week period of physical EE intervention. Behavioral testing was then conducted for 2 weeks. At this point, the study mice were about 3.5 months old. Therefore, this experimental protocol is available to investigate the impact of early-life SI on the onset of AD and to evaluate whether timely EE can correct or alleviate this exacerbating effect.

As previously stated, the synaptic development in mice is largely accomplished by about 3 weeks post-birth, with myelin development continuing into adulthood. By selecting 1.5-month-old 5×FAD mice for Arhgef7 overexpression or knockdown in mPFC neurons, the normal development and formation of synapses were not disrupted. Following viral treatment, the mice were kept for an additional three weeks, succeeded by a two-week behavioral testing period, by which time the mice had reached 11 weeks of age. This experimental protocol enables us to specifically delineate the effects of Arhgef7 overexpression on SI-5×FAD mice and the effects of Arhgef7 knockdown on GH-5×FAD mice in terms of cognitive and synaptic function.

SI has become a widespread societal issue due to structural disruptions caused by pandemics, wars, and other global crises [52]. The detrimental effects of SI on brain function are hypothesized to accelerate AD progression through various mechanisms [46]. For example, SI induces chronic stress states that activate the hypothalamic-pituitary-adrenal axis, leading to increased glucocorticoid levels. These levels impair synaptic plasticity, promote neuroinflammation, and disrupt myelination [53, 54]. Furthermore, SI may exacerbate AD-related pathology by suppressing brain-derived neurotrophic factor (BDNF) expression and increasing the production of pro-inflammatory cytokines, such as interleukin-6 [55]. Previous studies from our laboratory have shown that early-life SI triggers cognitive deficits, anxiety-like behavior, and social-cooperative impairments in mice,

with transgenerational effects observed in offspring [11, 56, 57]. In this study, we further demonstrate that early-life SI accelerates spatial cognitive decline, exacerbates anxiety-like behaviors, and impairs social interaction and cooperation skills in 5×FAD mice. Pathologically, SI aggravates synaptic dysfunction, dendritic spine loss, axonal structural damage, hypomyelination, and glial reactivity in the mPFC of 5×FAD mice. These findings are consistent with our earlier observations in young APP/PS1 mice [11], reinforcing the role of SI as a critical environmental factor that accelerates AD-related neurobehavioral and neuropathological deficits.

In contrast to SI, EE confers significant health benefits in both animals and humans [58]. Multisensory stimulations—such as tactile experiences (e.g., artistic creation), visual engagement (e.g., natural landscapes or artwork), and auditory stimuli (e.g., music)—have been shown to activate neural networks, enhance neuroplasticity, improve learning capacity, and facilitate emotional regulation [59–61]. Additionally, physical exercise, a critical component of EE, not only enhances cognitive function by promoting cerebral blood flow and increasing BDNF secretion but also mitigates neurodegenerative changes in brain structure and function in individuals with mild cognitive impairment [62, 63]. A growing body of research has explored the potential of EE as a non-pharmacological intervention for AD [64]. In the present study, the physical EE showed heterogeneous efficacy in early isolated AD mice: it restored spatial cognition, alleviated anxiety-like behaviors, and maintained neuronal axonal and dendritic integrity, yet it did not improve social behavioral deficits and hypomyelination.

Beyond enriched sensory stimulation and physical activity, social enrichment constitutes another critical component of EE that cannot be overlooked [58]. Social behavior serves as both a cornerstone of maintaining social operations and a key determinant in promoting the healthy development of individuals and collectives [65]. Social enrichment has been demonstrated to confer benefits such as improving cognitive function, enhancing emotional regulation, promoting mental and physical well-being, increasing life satisfaction, and reducing

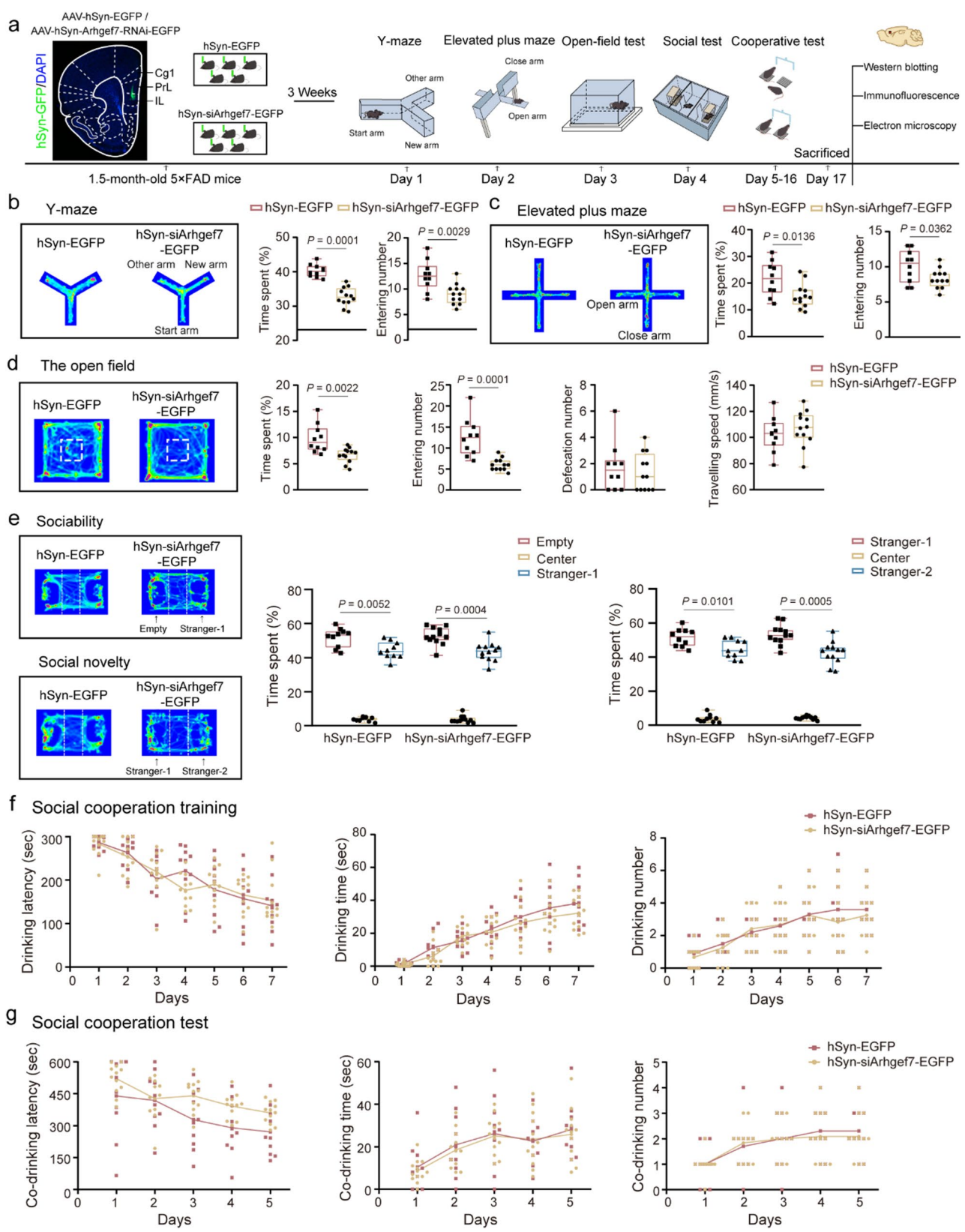


Fig. 6 (See legend on next page.)

(See figure on previous page.)

Fig. 6 Knocking down *Arhgef7* in the mPFC impaired cognitive function and increased anxiety-like behavior in 5×FAD mice. **A** Experimental design schematic. **B** Left: the heatmap showing the movement trajectory of 5×FAD mice in hSyn-EGFP group and hSyn-siArhgef7-EGFP group in the Y-maze test; Right: the percentage of time spent in and number of entries into the novel arm. **C** Left: the heatmap of mouse movement trajectories in the elevated plus maze test; Right: the percentage of time spent in and number of entries into the open arms. **D** Left: the heatmap of mouse movement trajectories in the open field test; Right: the percentage of time spent in the center area, number of entries into the center, fecal count, and travel speed. **E** Left: the heatmap of mouse trajectories during social preference and social memory tests in the three-chamber test; Right: the percentage of time spent in each chamber during the social preference and social memory tests. **F** The graphs showing latency to first drink, total drinking time, and number of drinking events during the training stage of the cooperative drinking water task. **G** The graphs showing latency to first drink, total co-drinking time, and number of co-drinking events during the testing stage of the cooperative drinking water task. hSyn-EGFP group, $n = 10$; hSyn-siArhgef7-EGFP group, $n = 12$ in (B–E). hSyn-EGFP, $n = 10$ pairs; hSyn-siArhgef7-EGFP group, $n = 12$ pairs in (G). Significant differences were assessed using two-tailed Student's *t*-tests. The data of cooperative drinking water test were analyzed by repeated-measures ANOVA and post hoc Student-Newman-Keuls test

the risk of dementia and other neurodegenerative disorders [66–68]. In individuals with AD, social withdrawal frequently manifests in early stages, characterized by reduced social interaction and avoidance of communal activities. This withdrawal exacerbates social competency deficits, thereby forming a vicious cycle that accelerates AD progression [69]. In our study, both GH-5×FAD mice and SI-5×FAD mice were housed in an EE with larger spaces and diverse stimuli; however, improved social interaction and cooperative behaviors were only observed in the GH-5×FAD mice. These results underscore the crucial role of social factors in sustaining social behavioral competence and highlight their indispensable contribution to combating the progression of AD. An ongoing study in our laboratory primarily suggests that resocializing SI-5×FAD mice with wild-type mice leads to improvements in social behaviors and myelination. Collectively, the social component of EE seems to be critical and irreplaceable in counteracting the progression of AD.

Moreover, studies from our laboratory and others have demonstrated that social living is essential for the formation and long-term maintenance of myelin, while higher-order brain functions, such as social interaction and cooperation, critically depend on normal myelin plasticity [18, 56]. In this study, histopathological analyses revealed that EE exerted protective effects on neuronal processes, synaptic integrity, and myelination in the mPFC of GH-5×FAD mice; however, it only restored mPFC neuronal plasticity in SI mice. Therefore, it is crucial to prevent SI in AD patients, maintain their existing social relationships, and enhance their social interactions throughout the prevention and treatment period.

On the other hand, myelination plays a distinct and essential role in regulating social behavior [70]. Disruptions in myelination within the mPFC may impair neural circuit integrity and temporal synchrony, thereby compromising the processing of social cues and appropriate behavioral responses [71–73]. Increasing evidence suggests that myelination is highly experience-dependent, with social interaction during critical developmental windows acting as a key modulator of myelin plasticity, although the specific mechanisms remain unclear [74]. Therefore, the social behavioral deficits observed in

young adult SI-5×FAD mice may, at least in part, result from persistent abnormalities in myelination.

The emergence of A β plaques is one of the earliest pathological hallmarks of AD, initiating a cascade of downstream neurodegenerative events. Consequently, the mechanisms of A β production and clearance remain central to AD research [75]. For example, our previous studies demonstrated that 3 months of SI exacerbates A β plaque burden in the hippocampus of aged APP/PS1 mice [76]. In the current study, we further found that early-life SI significantly exacerbated A β deposition in the mPFC of 5×FAD mice. Moreover, previous research from our laboratory indicates that 1-month-old APP/PS1 mice subjected to 8-week SI exhibit an increase in cortical and hippocampal A β deposition [11], likely because A β plaques in this AD model typically emerge at 5–6 months of age. In contrast, 5×FAD mice exhibit accelerated A β pathology, with plaque deposition starting as early as 1.5 months of age [77]. These differences underscore the importance of considering temporal and regional specificity in A β pathology when designing interventions for various stages of AD.

Intriguingly, the physical EE exhibited heterogeneous effects on A β deposition: it significantly reduced A β burden in the mPFC of GH-5×FAD mice but showed no efficacy in SI-5×FAD mice. A possible explanation for this phenomenon is that myelin also plays a crucial role in maintaining the homeostasis of brain A β . Recent studies suggest that myelin dysfunction or demyelination worsens A β accumulation [78], while appropriate myelin wrapping and healthy myelin initially inhibit plaque formation [79]. Thus, myelin damage induced by SI may counteract the benefits of the physical EE in clearing A β in SI-5×FAD mice, while EE's capacity to maintain myelin integrity in GH mice likely acts as a prerequisite for its protective effects against A β deposition.

Upon analyzing the transcriptomic data, we identified genes that were consistently up-regulated or down-regulated in both the GH and SI groups following the physical EE intervention. This enabled us to pinpoint key candidates that might enhance cognitive function. We discovered that alterations in the *Arhgef7* gene were associated with behavioral and pathological changes linked to SI and

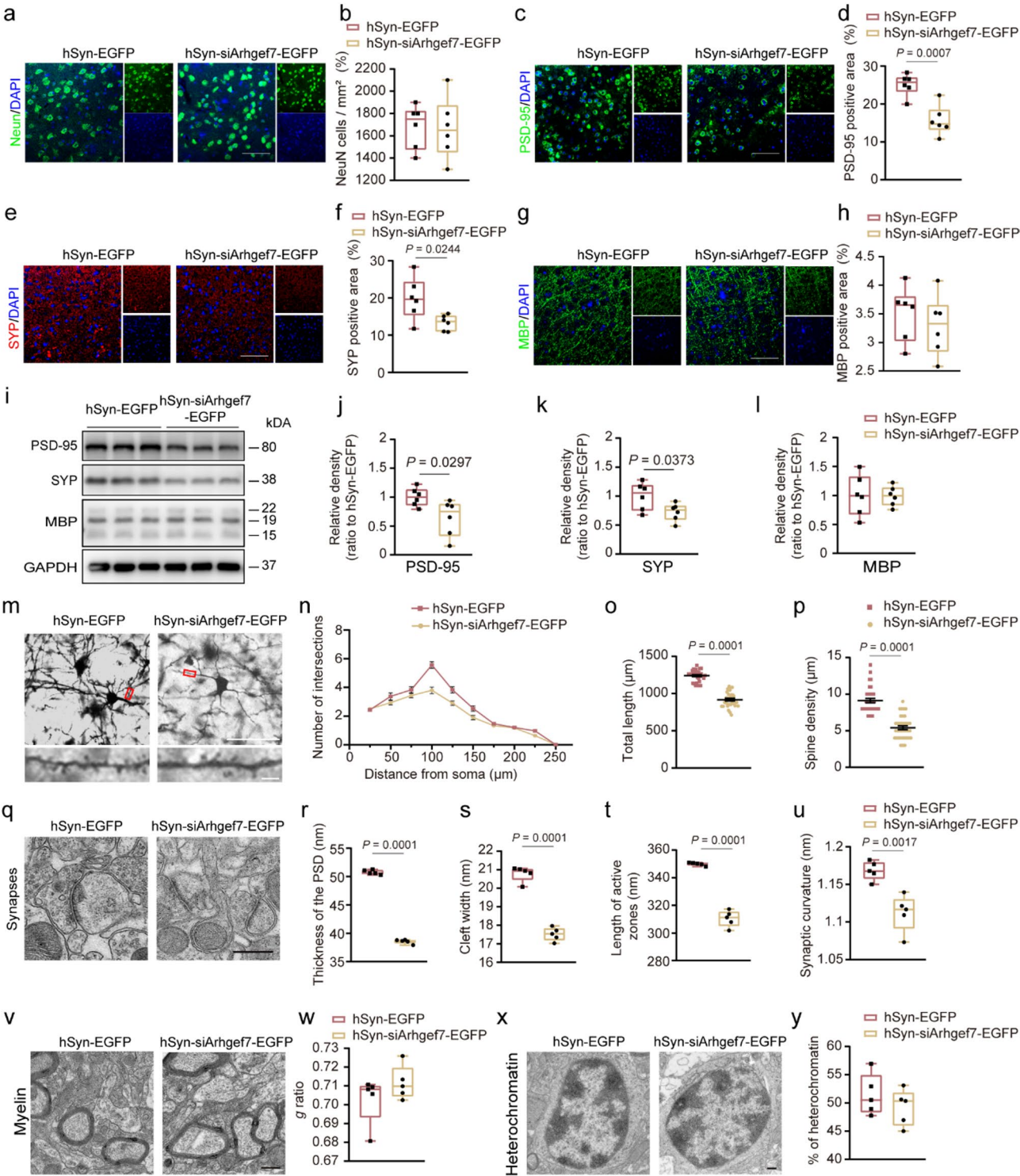


Fig. 7 (See legend on next page.)

EE exposure. Arhgef7 serves as a central node, exhibiting extensive connections with synaptic and cytoskeletal regulators. Its established biological functions are directly associated with processes pertinent to our phenotypes of interest, such as synaptic structure, inhibitory

neurotransmission, and axonal integrity. In comparison, other candidates within the network either had limited prior functional annotations related to AD-relevant pathways or displayed less consistent regulation across different datasets.

(See figure on previous page.)

Fig. 7 Arhgef7 knockdown impaired dendritic and synaptic structures but not myelin sheath integrity in the mPFC. **A–H** Representative images of immunofluorescence for NeuN (A), PSD-95 (C), SYP (E), MBP (G) of 5×FAD mice in hSyn-EGFP group and hSyn-siArhgef7-EGFP group. Scale bar: 50 μ m. And the number of NeuN positive neurons per unit area (B), statistical analysis of the PSD-95 positive area (D), SYP positive area (F), MBP positive area (H), ($n=6$). **I** Representative Western blot bands of PSD-95, SYP, and MBP of the two groups. **J–L** The gray values of bands for PSD-95 (J), SYP (K), and MBP (L) ($n=6$). **M** Golgi staining showed neurite complexity and dendrite spine density of the two groups. Scale bar: neurite 50 μ m, dendritic spine 2 μ m. **N** The distribution of dendrite length with distance from the cell body. Each group consists of 6 mice, with 5 neurons counted for each mouse. **O** The total length of neurites in the two groups. **P** Density of dendritic spines. The data came from six mice in each group, each with six dendritic spines. **Q** Representative EM images showing synaptic morphology in the two groups. Scale bar, 500 nm. **R–U** Quantification of PSD, synaptic cleft width, active zone length, and synaptic curvature in hSyn-EGFP group and hSyn-siArhgef7-EGFP group. 75 synapses per mouse, $n=5$ mice per group. **V** Representative EM images showing myelin sheath in the two groups. Scale bar, 500 nm. **W** The scatterplot of myelin g-ratio in hSyn-EGFP group (110 axons) and hSyn-siArhgef7-EGFP group (112 axons) ($n=5$). **X** Representative EM images showing OLs nuclear heterochromatin in the two groups. Scale bar, 500 nm. **Y** The area percentage of OLs nuclear heterochromatin in the two groups. 25 synapses per mouse, $n=5$ mice per group. Significant differences were assessed using two-tailed Student's *t*-tests

Arhgef7 encodes a guanine nucleotide exchange factor (GEF) for CDC42 and Rac1, belonging to the cytoplasmic protein family. It activates Ras-like Rho GTPases by catalyzing the exchange of bound GDP for GTP [80]. This protein regulates diverse biological processes, including cytoskeletal remodeling, cell migration, intracellular signaling, and synaptic development [81, 82]. Notably, it functions as a scaffolding protein for gamma-aminobutyric acid (GABA) receptor localization, playing a pivotal role in maintaining synaptic integrity and axonal function [83]. GABA, the primary inhibitory neurotransmitter, modulates the excitatory-inhibitory balance in the brain and is essential for neural network stability and synaptic plasticity. However, patients with AD often exhibit impaired GABA receptor function, leading to reduced neural inhibition, which is closely associated with cognitive impairment [84, 85]. Restoring GABAergic signaling has shown promise in reversing early-stage cognitive deficits in AD [86]. Simultaneously, stress-induced hyperactivity exacerbates GABA receptor dysfunction [87].

The experimental results indicate that the overexpression of Arhgef7 in mPFC neurons leads to an increase in dendritic spine density and synaptic complexity in SI-5×FAD mice, which is accompanied by improved cognitive performance and a reduction in anxiety-like behaviors. These positive outcomes may be attributed to enhanced GABA receptor function, rather than alterations in A β plaque load. Interestingly, previous research has shown that Arhgef7 heterozygous mice display impaired social interaction, and a decrease in Arhgef7 protein expression is associated with deficits in social behavior [88]. However, in this study, neither knockdown nor overexpression of the *Arhgef7* gene in mPFC neurons significantly altered social behaviors in mice. This may be due to our intervention being limited to the mPFC region of the brain, without affecting the functionality of other brain areas. Additionally, we specifically targeted Arhgef7 in neuronal cells, rather than conducting a complete knockdown of Arhgef7, which may also lead to different regulatory effects on social behavior.

Signaling pathways that regulate synaptic plasticity play a pivotal role in maintaining neurological function.

Numerous studies have shown the involvement of multiple pathways in modulating synaptic plasticity, and their roles in resisting AD-related pathology have become increasingly prominent. In the nervous system, the Wnt pathway regulates synaptic plasticity, neuroprotection, and repair, critically influencing neuronal growth, maintenance, and remodeling. Dysregulation of Wnt signaling is closely associated with core AD pathologies, including tau hyperphosphorylation, A β plaque accumulation, synaptic dysfunction, and cognitive deficits [43, 89, 90]. In our study, SI increased β -catenin phosphorylation in the mPFC of 5×FAD mice. We identified that overexpressing Arhgef7 counteracts A β toxicity by suppressing β -catenin phosphorylation, thereby activating Wnt signaling and promoting synaptogenesis. This clue suggests that the regulation of Wnt signaling by Arhgef7 is implicated in the physical EE resistance to AD pathology.

Notably, our previous studies demonstrated that 8-week of the physical EE failed to ameliorate synaptic impairments in the mPFC of 1-month-old SI-CD1 mice [91]. In contrast, our study observed that 3 weeks of the physical EE significantly improved synaptic function in 3.5-month-old 5×FAD mice previously subjected to 3-week SI. In normally developing mice, the neuronal dendrites and axons maintain thriving plasticity. In contrast, 5×FAD mice exhibit synaptic dysfunction, which worsens with progressive A β accumulation [92, 93]. This discrepancy indicates that the degree of damage to the neural networks caused by SI may vary among different conditions, leading to differences in their sensitivity to the physical EE interventions. In addition, as described above, oligodendrocyte maturation and myelination play critical roles in regulating social memory and cooperative behaviors [56, 94, 95]. On the other hand, the maintenance of myelin sheaths in social animals, including humans, is highly dependent on normal social activities.

In line with this perspective, the findings of this study indicate that merely enhancing the physical environment or restoring the plasticity of neuronal processes cannot rectify the damage to myelin sheaths inflicted by SI. Our previous work identified early growth response 2 (Egr2) in mPFC oligodendrocytes as a key regulator

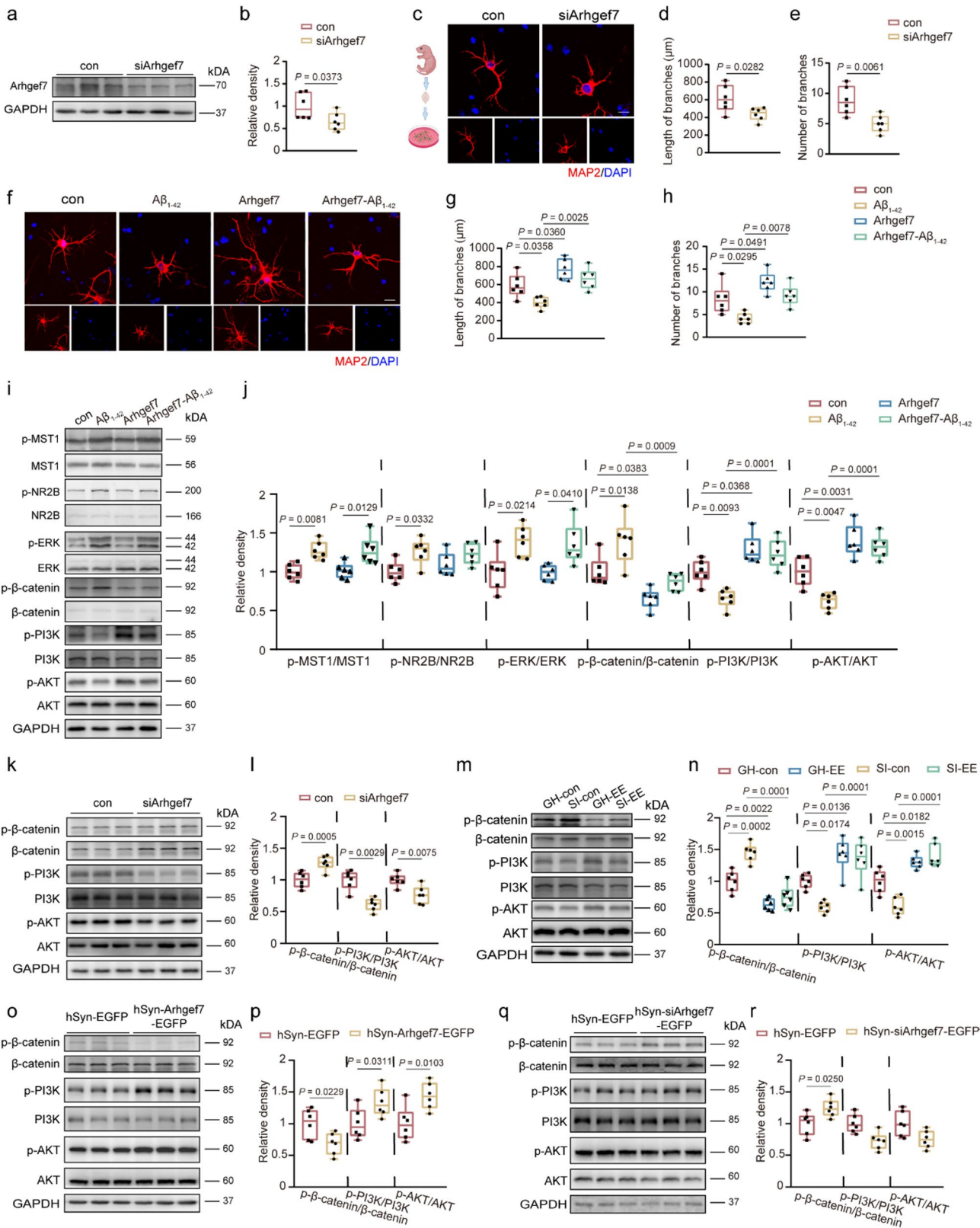


Fig. 8 (See legend on next page.)

(See figure on previous page.)

Fig. 8 Arhgef7 promoted primary neurite growth and modulated $A\beta_{1-42}$ toxicity via Wnt signaling pathways. **A** Western blot analysis showing successful knockdown of Arhgef7 expression in primary cortical neurons by siRNA. **B** The gray values of bands for Arhgef7 ($n=6$). **C-E** Representative images of dendrites from primary cortical neurons cultured from Control (NC) and siArhgef7 groups (C), along with quantitative analysis of dendrite length (D) and branching number (E). Scale bar: 20 μ m. **F-H** Primary cortical neurons from mice in NC and siArhgef7 groups were treated with $A\beta_{1-42}$ (10 μ M) for 24 h. Representative MAP2 immunofluorescence images of dendrites (F) and quantitative analysis of dendrite length (G) and branching number for each group (H). Scale bar: 20 μ m. **I-J** Representative Western blot bands and statistical analysis of MST1, p-MST1, NR2B, p-NR2B, ERK, p-ERK, β -catenin, p- β -catenin, PI3K, p-PI3K, AKT, and p-AKT in primary cortical neurons. ($n=6$ per group). **K-L** Western blot bands and statistical analysis of β -catenin, p- β -catenin, PI3K, p-PI3K, AKT, and p-AKT in siRNA-treated primary cortical neurons ($n=6$). **M-N** Representative Western blot bands and statistical analysis of β -catenin, p- β -catenin, PI3K, p-PI3K, AKT, and p-AKT in the mPFC of GH-con, SI-con, GH-EE, and SI-EE groups of mice ($n=6$). **O-P** Representative Western blot bands and statistical analysis of β -catenin, p- β -catenin, PI3K, p-PI3K, AKT, and p-AKT in the mPFC of SI-hSyn-EGFP and SI-hSyn-Arhgef7-EGFP groups of mice ($n=6$). **Q-R** Representative Western blot bands and statistical analysis of β -catenin, p- β -catenin, PI3K, p-PI3K, AKT, and p-AKT in the mPFC of hSyn-EGFP and hSyn-siArhgef7-EGFP groups of mice ($n=8$). Significant differences were assessed using unpaired two-tailed Student's t-tests (B, D, E, L, P, R) and two-way ANOVA followed by Tukey's post hoc test (G, H, J, N), respectively

of social interaction and cooperative deficits in SI mice [56]. The transcription factor Egr2 is proposed as a potential upstream regulator of miRNA expression in 15-month-old APP/PS1 mice. Egr2's involvement in both transcriptional and epigenetic regulation suggests it may contribute to AD-related transcriptomic remodeling by modulating non-coding RNA networks. Importantly, Egr2 dysregulation could underline the observed demyelination and social deficits in AD, positioning it as a critical node connecting myelin integrity, behavioral dysfunction, and neurodegenerative pathology [96]. However, whether regulating Egr2 is involved in the exacerbating effect of early SI on myelin degeneration in the AD process remains to be determined.

The current study has several limitations. Both male and female 5 \times FAD mice were used, but the data was not stratified by sex. The reanalysis of the behavioral data uncovered trends in sex-related differences; however, these differences did not reach statistical significance, except for the number of entries into the open arms during the EPM test (Figures S5). Future research necessitates larger sample sizes to clarify the potential influence of gender factors on the interaction between social and environmental factors in the pathogenesis of AD.

In addition, our *in vivo* data suggest correlations rather than direct causal relationships between Arhgef7 and the Wnt/PI3K signaling pathways. It remains unclear whether the Wnt/PI3K signaling operates downstream of Arhgef7 or if it represents a parallel mechanism that is independently activated by the physical EE. Nevertheless, further research involving targeted genetic or pharmacological manipulation of Wnt/PI3K components, both in the presence and absence of Arhgef7, is necessary to clarify their precise relationship.

Moreover, while the mPFC is pivotal in social behavior, the process is intricate and involves the concerted efforts of various brain regions, such as the anterior cingulate cortex, amygdala, and striatum. Each of these regions also plays a critical role in emotional processing, reward valuation, and social motivation [97–99]. Consequently, alterations in Arhgef7 that occur exclusively within the mPFC may not be sufficient to substantially modify

overall social ability. Dysfunction in any of these brain regions may contribute to persistent social impairments. Thus, future strategies aiming to restore social behavior may require broader, multi-regional interventions that target key hubs within the social brain network, extending beyond the mPFC.

Conclusion

This study focused on the AD-like early stages, incorporating environmental and social factors, and explored the impact of the physical EE on the behavioral pathology of early-life isolated 5 \times FAD mice. The results indicate that early-life SI has a detrimental effect on spatial cognition, anxiety levels, social interaction, and cooperative behavior in the early stages of AD, while the physical EE can only have a corrective effect on the first two. The pathological results have revealed that the physical EE can mitigate SI-induced alterations in synapses rather than myelin sheaths in the mPFC. Our study also identified Arhgef7 as a key mediator of the beneficial effects of physical stimuli on spatial cognition, emotion, and neuronal processes in the mPFC, potentially via the Wnt signaling pathway. Collectively, this work provides evidence supporting the use of the physical EE as a non-pharmacological strategy to delay cognitive decline in early AD and proposes Arhgef7 as a novel therapeutic target for early intervention and treatment.

Abbreviations

AAV	Adeno-associated virus
AD	Alzheimer's disease
$A\beta$	Amyloid β -protein
Arhgef7	Rho guanine nucleotide exchange factor 7
BDNF	Brain-derived neurotrophic factor
EE	Enriched environment
ESyt1	Extended Synaptotagmin 1
GABA	Gamma-Aminobutyric Acid
GFAP	Glial fibrillary acidic protein
GAPDH	Glyceraldehyde-3-phosphate dehydrogenase
GH	group-housed
HPA	Hypothalamic-pituitary-adrenal
Iba1	Ionized calcium-binding adapter molecule 1
IL-6	Interleukin-6
Kv4.2	Potassium voltage-gated channel subfamily D member 2
MAP2	Microtubule-associated protein 2
MBP	Myelin basic protein
mPFC	Medial prefrontal cortex

NeuN	Neuronal nuclear antigen
PPI	Protein-protein interaction
PSD-95	Postsynaptic density protein-95
qPCR	Quantitative real-time PCR
RNA-seq	RNA sequencing
shRNA	Short hairpin RNA
SI	Social isolation
SYP	Synaptophysin

Supplementary Information

The online version contains supplementary material available at <https://doi.org/10.1186/s13195-025-01797-5>.

Supplementary Material 1

Acknowledgements

Not applicable.

Author contributions

M.X., and Y.Z. conceived and conducted the project. M.X., Y.Z., and J.G. supervised the project. M.X., Y.Z., and Y.W. wrote the paper. Y.W., Z.W., M.C., S.C. S.D., S.Z., and Y.L. performed the experiments and data analysis. Z.W., Y.J., and S.D. contributed to mouse models and cell culture. Y.Z., Y.W., Z.W., S.C., and S.D. contributed to imaging analysis and interpreted the data.

Funding

This work was supported by the National Natural Science Foundation of China (82304466 and 82204365); the Natural Science Foundation of Jiangsu Province (BK20241869) and Postgraduate Research & Practice Innovation Program of Jiangsu Province (JX10114225 and JX10114233).

Data availability

No datasets were generated or analysed during the current study.

Declarations

Ethics approval and consent to participate

All procedures in this study were performed according to the protocol reviewed and approved by the Nanjing Medical University Animal Care and Use Committee.

Consent for publication

Not applicable.

Competing interests

The authors declare no competing interests.

Author details

¹Jiangsu Key Laboratory of Neurodegeneration, Nanjing Medical University, Nanjing 211166, China

²Wuxi People's Hospital, Wuxi Medical Center, Nanjing Medical University, Wuxi 214000, China

Received: 11 May 2025 / Accepted: 23 June 2025

Published online: 01 July 2025

References

1. Brody H. Alzheimer's disease. *Nature*. 2011;475:31.
2. van der Wee NJA, Bilderbeck AC, Cabello M, Ayuso-Mateos JL, Saris IMJ, Giltay EJ, et al. Working definitions, subjective and objective assessments and experimental paradigms in a study exploring social withdrawal in schizophrenia and Alzheimer's disease. *Neurosci Biobehav Rev*. 2019;97:38–46.
3. Salloway S. Current and future treatments for Alzheimer's disease. *CNS Spectr*. 2009;14:4–7. discussion 16–8.
4. Brandt L, Liu S, Heim C, Heinz A. The effects of social isolation stress and discrimination on mental health. *Transl Psychiatry*. 2022;12:398.
5. Sommerlad A, Kivimaki M, Larson EB, Rohr S, Shirai K, Singh-Manoux A, et al. Social participation and risk of developing dementia. *Nat Aging*. 2023;3:532–45.
6. Xiong Y, Hong H, Liu C, Zhang YQ. Social isolation and the brain: effects and mechanisms. *Mol Psychiatry*. 2023;28:191–201.
7. Nithianantharajah J, Hannan AJ. Enriched environments, experience-dependent plasticity and disorders of the nervous system. *Nat Rev Neurosci*. 2006;7:697–709.
8. van Praag H, Kempermann G, Gage FH. Neural consequences of environmental enrichment. *Nat Rev Neurosci*. 2000;1:191–8.
9. Komitova M, Mattsson B, Johansson BB, Eriksson PS. Enriched environment increases neural stem/progenitor cell proliferation and neurogenesis in the subventricular zone of stroke-lesioned adult rats. *Stroke*. 2005;36:1278–82.
10. Xu YQ, Chen Y, Xing JX, Yao J. Relationship between enriched environment and neurodegeneration: a review from mechanism to therapy. *Clin Epigenetics*. 2025;17:13.
11. Cao M, Hu PP, Zhang YL, Yan YX, Shields CB, Zhang YP, et al. Enriched physical environment reverses spatial cognitive impairment of socially isolated APPswe/PS1dE9 transgenic mice before amyloidosis onset. *CNS Neurosci Ther*. 2018;24:202–11.
12. Amador P, Lopez M, Cuesta-Lopez I, Jove Cs, Begega A. Pro-resilient effects of environmental enrichment on social isolation: behavioural and cytochrome c oxidase brain analysis in Wistar adult rats. *Behav Brain Res*. 2025;487:115574.
13. Morici JF, Bekinschtein P, Weisstaub NV. Medial prefrontal cortex role in recognition memory in rodents. *Behav Brain Res*. 2015;292:241–51.
14. Lindberg O, Westman E, Karlsson S, Ostberg P, Svensson LA, Simmons A, et al. Is the subcallosal medial prefrontal cortex a common site of atrophy in Alzheimer's disease and frontotemporal lobar degeneration? *Front Aging Neurosci*. 2012;4:32.
15. Komori T, Okamura K, Ikehara M, Yamamuro K, Endo N, Okumura K, et al. Brain-derived neurotrophic factor from microglia regulates neuronal development in the medial prefrontal cortex and its associated social behavior. *Mol Psychiatry*. 2024;29:1338–49.
16. Zhang M, Li X, Zhuo S, Yang M, Yu Z. Enriched environment enhances sociability through the promotion of ESyt1-related synaptic formation in the medial prefrontal cortex. *Mol Neurobiol*. 2024;61:3019–30.
17. Lodha J, Brocato E, Wolstenholme JT. Areas of convergence and divergence in adolescent social isolation and binge drinking: a review. *Front Behav Neurosci*. 2022;16:859239.
18. Thamizhoviya G, Vanisree AJ. Enriched environment modulates behavior, myelination and augments molecules governing the plasticity in the fore-brain region of rats exposed to chronic immobilization stress. *Metab Brain Dis*. 2019;34:875–87.
19. Shin MS, Song SH, Shin JE, Lee SH, Huh SO, Park D. Src-mediated phosphorylation of betaPix-b regulates dendritic spine morphogenesis. *J Cell Sci*. 2019;132.
20. Kwon Y, Lee SJ, Shin YK, Choi JS, Park D, Shin JE. Loss of neuronal betapix isoforms impairs neuronal morphology in the hippocampus and causes behavioral defects. *Anim Cells Syst (Seoul)*. 2025;29:57–71.
21. Liaci C, Camera M, Caslini G, Rando S, Contino S, Romano V, et al. Neuronal cytoskeleton in intellectual disability: from systems biology and modeling to therapeutic opportunities. *Int J Mol Sci*. 2021;22.
22. Bhambhani HP, Mueller TM, Simmons MS, Meador-Woodruff JH. Actin polymerization is reduced in the anterior cingulate cortex of elderly patients with schizophrenia. *Transl Psychiatry*. 2017;7:1278.
23. Liu L, Yuan H, Yi Y, Koellhoffer EC, Munshi Y, Bu F, et al. Ras-related C3 botulinum toxin substrate 1 promotes axonal regeneration after stroke in mice. *Transl Stroke Res*. 2018;9:506–14.
24. Fuchsova B, Alvarez Julia A, Rizavi HS, Frasch AC, Pandey GN. Expression of p21-activated kinases 1 and 3 is altered in the brain of subjects with depression. *Neuroscience*. 2016;333:331–44.
25. Garofalo S, Cocozza G, Mormino A, Bernardini G, Russo E, Ielpo D, et al. Natural killer cells and innate lymphoid cells 1 tune anxiety-like behavior and memory in mice via interferon-gamma and acetylcholine. *Nat Commun*. 2023;14:3103.
26. Walf AA, Frye CA. The use of the elevated plus maze as an assay of anxiety-related behavior in rodents. *Nat Protoc*. 2007;2:322–8.
27. Eo H, Lee S, Kim SH, Ju IG, Huh E, Lim J, et al. Petasites japonicus leaf extract inhibits Alzheimer's-like pathology through suppression of neuroinflammation. *Food Funct*. 2022;13:10811–22.

28. Feng W, Zhang Y, Wang Z, Wang T, Pang Y, Li Y, et al. Protocol for evaluating mutualistic cooperative behavior in mice using a water-reward task assay. *STAR Protoc.* 2024;5:103023.
29. Bacskai BJ, Kajdasz ST, Christie RH, Carter C, Games D, Seubert P, et al. Imaging of amyloid-beta deposits in brains of living mice permits direct observation of clearance of plaques with immunotherapy. *Nat Med.* 2001;7:369–72.
30. Zhao S, Chen Y, Chen F, Huang D, Shi H, Lo LJ, et al. Sas10 controls ribosome biogenesis by stabilizing Mpp10 and delivering the Mpp10-Imp3-Imp4 complex to nucleolus. *Nucleic Acids Res.* 2019;47:2996–3012.
31. Ma X, Wang Y, Li W, Wang K, Zhang S. Bisphenol A disrupts ribosome function during ovarian development of mice. *Toxics.* 2024;12.
32. Richier L, Williton K, Clattenburg L, Colwill K, O'Brien M, Tsang C, et al. NOS1AP associates with scribble and regulates dendritic spine development. *J Neurosci.* 2010;30:4796–805.
33. Zhu D, Zhang J, Gao F, Hu M, Hashem J, Chen C. Augmentation of 2-arachidonoylglycerol signaling in astrocytes maintains synaptic functionality by regulation of miRNA-30b. *Exp Neurol.* 2023;361:114292.
34. Yuan L, Yi W, Sun C, Ma S, Wang J, Liu S, et al. EphB2 activates CREB-dependent expression of Annexin A1 to regulate dendritic spine morphogenesis. *Biochem Biophys Res Commun.* 2021;584:107–15.
35. Park E, Na M, Choi J, Kim S, Lee JR, Yoon J, et al. The Shank family of postsynaptic density proteins interacts with and promotes synaptic accumulation of the beta PIX guanine nucleotide exchange factor for Rac1 and Cdc42. *J Biol Chem.* 2003;278:19220–9.
36. Kim S, Park H, Kang J, Choi S, Sadra A, Huh SO. beta-PIX-d, a member of the ARHGEF7 guanine nucleotide exchange factor family, activates Rac1 and induces neuritogenesis in primary cortical neurons. *Exp Neurobiol.* 2024;33:215–24.
37. Jeon Y, Shin YK, Kim H, Choi YY, Kang M, Kwon Y et al. BetaPix guanine nucleotide exchange factor regulates regeneration of injured peripheral axons. *Int J Mol Sci.* 2023;24.
38. Ge TQ, Guan PP, Wang P. Complement 3a induces the synapse loss via C3aR in mitochondria-dependent NLRP3 activating mechanisms during the development and progression of Alzheimer's disease. *Neurosci Biobehav Rev.* 2024;165:105868.
39. Wang H, Shang Y, Wang E, Xu X, Zhang Q, Qian C, et al. MST1 mediates neuronal loss and cognitive deficits: a novel therapeutic target for Alzheimer's disease. *Prog Neurobiol.* 2022;214:102280.
40. Li Y, Wu H, Liu M, Zhang Z, Ji Y, Xu L, et al. Polysaccharide from *Polygala tenuifolia* alleviates cognitive decline in Alzheimer's disease mice by alleviating Abeta damage and targeting the ERK pathway. *J Ethnopharmacol.* 2024;321:117564.
41. Zhang B, Zhao J, Yan C, Bai Y, Guo P, Wang C, et al. Combination of RNA-seq and proteomics reveals the mechanism of DL0410 treatment in APP/PS1 transgenic mouse model of Alzheimer's disease. *Biomed Pharmacother.* 2024;177:116940.
42. He Y, Wang Y, Li X, Qi Y, Qu Z, Hu Y. Lycium barbarum polysaccharides improves cognitive functions in ICV-STZ-induced Alzheimer's disease mice model by improving the synaptic structural plasticity and regulating IRS1/PI3K/AKT signaling pathway. *Neuromolecular Med.* 2024;26:15.
43. Shi T, Shen S, Shi Y, Wang Q, Zhang G, Lin J, et al. Osteocyte-derived sclerostin impairs cognitive function during ageing and Alzheimer's disease progression. *Nat Metab.* 2024;6:531–49.
44. Fortea J, Vague-Alcazar L, Pegueroles J, Alcolea D, Belbin O, Dols-Icardo O, et al. Reply to: challenges to identifying risk versus protective factors in Alzheimer's disease. *Nat Med.* 2024;30:3096–7.
45. Mertas B, Bosgelmez II. The role of genetic, environmental, and dietary factors in Alzheimer's disease: a narrative review. *Int J Mol Sci.* 2025;26.
46. Hsiao YH, Chen PS, Chen SH, Gean PW. The involvement of Cdk5 activator p35 in social isolation-triggered onset of early Alzheimer's disease-related cognitive deficit in the transgenic mice. *Neuropsychopharmacology.* 2011;36:1848–58.
47. Livingston G, Huntley J, Sommerlad A, Ames D, Ballard C, Banerjee S, et al. Dementia prevention, intervention, and care: 2020 report of the lancet commission. *Lancet.* 2020;396:413–46.
48. Dubois J, Dehaene-Lambertz G, Kulikova S, Poupon C, Huppi PS, Hertz-Pannier L. The early development of brain white matter: a review of imaging studies in fetuses, newborns and infants. *Neuroscience.* 2014;276:48–71.
49. Oakley H, Cole SL, Logan S, Maus E, Shao P, Craft J, et al. Intraneuronal beta-amyloid aggregates, neurodegeneration, and neuron loss in transgenic mice with five familial Alzheimer's disease mutations: potential factors in amyloid plaque formation. *J Neurosci.* 2006;26:10129–40.
50. Locci A, Orellana H, Rodriguez G, Gottliebson M, McClarty B, Dominguez S, et al. Comparison of memory, affective behavior, and neuropathology in APP(NLGF) knock-in mice to 5xFAD and APP/PS1 mice. *Behav Brain Res.* 2021;404:113192.
51. Kosel F, Torres Munoz P, Yang JR, Wong AA, Franklin TB. Age-related changes in social behaviours in the 5xFAD mouse model of Alzheimer's disease. *Behav Brain Res.* 2019;362:160–72.
52. Huang F, Liu X, Guo Q, Mahaman YAR, Zhang B, Wang JZ, et al. Social isolation impairs cognition via Abeta-mediated synaptic dysfunction. *Transl Psychiatry.* 2024;14:380.
53. Leitze O, Francis-Oliveira J, Khedr SM, Ariste L, Robel S, Kano SI, et al. Adolescent stress accelerates postpartum novelty recognition impairment in 5xFAD mice. *Front Neurosci.* 2024;18:1366199.
54. Rullo L, Losapio LM, Morosini C, Mottarlini F, Schiavi S, Buzzelli V, et al. Outcomes of early social experiences on glucocorticoid and endocannabinoid systems in the prefrontal cortex of male and female adolescent rats. *Front Cell Neurosci.* 2023;17:1270195.
55. Trachtenberg E, Ruzal K, Sandbank E, Bigelman E, Ricon-Becker I, Cole SW, et al. Deleterious effects of social isolation on neuroendocrine-immune status, and cancer progression in rats. *Brain Behav Immun.* 2025;123:524–39.
56. Zhang Y, Feng W, Wang Z, Pang Y, Jin Y, Chen S, et al. Early growth response 2 in the mPFC regulates mouse social and cooperative behaviors. *Lab Anim (NY).* 2023;52:37–50.
57. Chen S, Ding S, Pang Y, Jin Y, Sun P, Li Y, et al. Dysregulated miR-124 mediates impaired social memory behavior caused by paternal early social isolation. *Transl Psychiatry.* 2024;14:392.
58. Law M, Jarrett P, Nater UM, Skoluda N, Broadbent E. The effects of environmental enrichment on skin barrier recovery in humans: a randomised trial. *Sci Rep.* 2020;10:9829.
59. Bonthoux S, Chollet S. Wilding cities for biodiversity and people: a transdisciplinary framework. *Biol Rev Camb Philos Soc.* 2024;99:1458–80.
60. Dong J, Dong Y, An L, Wang Y, Li Y, Jin L. The role of the sensory input intervention in recovery of the motor function in hypoxic ischemic encephalopathy rat model. *J Neurophysiol.* 2024;131:865–71.
61. Liu T, Gray-Bauer H, Davison KE, Zuk J. Preschoolers' home music environment relates to their home literacy environment and parental self-efficacy. *PLoS ONE.* 2024;19:e0313218.
62. Gholami F, Mesrabadi J, Iranpour M, Donyaei A. Exercise training alters resting brain-derived neurotrophic factor concentration in older adults: a systematic review with meta-analysis of randomized-controlled trials. *Exp Gerontol.* 2025;199:112658.
63. Xu J, Yu J, Li G, Wang Y. Exercise intervention on the brain structure and function of patients with mild cognitive impairment: systematic review based on magnetic resonance imaging studies. *Front Psychiatry.* 2024;15:1464159.
64. Nam Y, Kim S, Park YH, Kim BH, Shin SJ, Leem SH, et al. Investigating the impact of environmental enrichment on proteome and neurotransmitter-related profiles in an animal model of Alzheimer's disease. *Aging Cell.* 2024;23:e14231.
65. Holt-Lunstad J, Smith TB, Layton JB. Social relationships and mortality risk: a meta-analytic review. *PLoS Med.* 2010;7:e1000316.
66. Hou P. Influence mechanism of internet use on the physical and mental health of the Chinese elderly-based on Chinese general social survey. *PLoS ONE.* 2025;20:e0312664.
67. Fridberg H, Wiklund M, Snellman F, Rosendahl E, Hedlund M, Boraxbekk CJ, et al. Negotiating a physically active life in tune with ageing: a grounded theory study of older persons' experiences of participating in high-intensity interval training. *BMC Geriatr.* 2025;25:11.
68. Tiley K, Crellin R, Domun T, Harkness F, Blodgett JM. Effectiveness of 234 interventions to improve life satisfaction: a rapid systematic review. *Soc Sci Med.* 2025;366:117662.
69. Bilderbeck AC, Penninx B, Arango C, van der Wee N, Kahn R, Winter-van Rossum I, et al. Overview of the clinical implementation of a study exploring social withdrawal in patients with schizophrenia and Alzheimer's disease. *Neurosci Biobehav Rev.* 2019;97:87–93.
70. Gong H, Lu Y, Deng SL, Lv KY, Luo J, Luo Y, et al. Targeting S100A9 attenuates social dysfunction by modulating neuroinflammation and myelination in a mouse model of autism. *Pharmacol Res.* 2025;211:107568.
71. Bonnefil V, Dietz K, Amatruda M, Wentling M, Aubry AV, Dupree JL et al. Region-specific myelin differences define behavioral consequences of chronic social defeat stress in mice. *Elife.* 2019;8.

72. Battulga B, Osanai Y, Yamazaki R, Shinohara Y, Ohno N. Axonal selectivity of myelination by single oOligodendrocytes established during development in mouse cerebellar white matter. *Glia*. 2025;73:873–86.
73. Pajevic S, Plenz D, Bassar PJ, Fields RD. Oligodendrocyte-mediated myelin plasticity and its role in neural synchronization. *Elife*. 2023;12.
74. Xin W, Kaneko M, Roth RH, Zhang A, Nocera S, Ding JB, et al. Oligodendrocytes and myelin limit neuronal plasticity in visual cortex. *Nature*. 2024;633:856–63.
75. Pichet Binette A, Gaiteri C, Wennstrom M, Kumar A, Hristovska I, Spotorno N, et al. Proteomic changes in Alzheimer's disease associated with progressive Abeta plaque and Tau tangle pathologies. *Nat Neurosci*. 2024;27:1880–91.
76. Huang H, Wang L, Cao M, Marshall C, Gao J, Xiao N, et al. Isolation housing exacerbates Alzheimer's disease-like pathophysiology in aged APP/PS1 mice. *Int J Neuropsychopharmacol*. 2015;18:pyu116.
77. Forner S, Kawauchi S, Balderrama-Gutierrez G, Kramar EA, Matheos DP, Phan J, et al. Systematic phenotyping and characterization of the 5xFAD mouse model of Alzheimer's disease. *Sci Data*. 2021;8:270.
78. Wood H. Myelin damage links brain ageing to amyloid-beta deposition. *Nat Rev Neurol*. 2023;19:457.
79. Depp C, Sun T, Sasmita AO, Spieth L, Berghoff SA, Nazarenko T, et al. Myelin dysfunction drives amyloid-beta deposition in models of Alzheimer's disease. *Nature*. 2023;618:349–57.
80. Matsuki T, Tabata H, Ueda M, Ito H, Nagata KI, Tsuneura Y et al. The MCPH7 gene product STIL is essential for dendritic spine formation. *Cells*. 2025;14.
81. Campa F, Machuy N, Klein A, Rudel T. A new interaction between Abi-1 and betapix involved in PDGF-activated actin cytoskeleton reorganisation. *Cell Res*. 2006;16:759–70.
82. Wang L, Pang K, Zhou L, Cebrian-Silla A, Gonzalez-Granero S, Wang S, et al. A cross-species proteomic map reveals neoteny of human synapse development. *Nature*. 2023;622:112–9.
83. Smith KR, Davenport EC, Wei J, Li X, Pathania M, Vaccaro V, et al. GIT1 and betapix are essential for GABA(A) receptor synaptic stability and inhibitory neurotransmission. *Cell Rep*. 2014;9:298–310.
84. Zhu W, Huang L, Cheng H, Li N, Zhang B, Dai W, et al. GABA and its receptors' mechanisms in the treatment of insomnia. *Heliyon*. 2024;10:e40665.
85. Backstrom T, Turkmen S, Das R, Doverskog M, Blackburn TP. The GABA system, a new target for medications against cognitive impairment-associated with neuroactive steroids. *J Intern Med*. 2023;294:281–94.
86. Bernardo AM, Marcotte M, Wong K, Sharmin D, Pandey KP, Cook JM, et al. Procognitive and neurotrophic benefits of alpha5-GABA-A receptor positive allosteric modulation in a beta-amyloid deposition mouse model of Alzheimer's disease pathology. *Neurobiol Aging*. 2025;147:49–59.
87. Harding SM, Van Dyke AR, Little M, LaClair MG. Sex differences in behavior and glutamic acid decarboxylase in long Evans rats after prolonged social isolation beginning in adolescence. *Behav Neurosci*. 2024;138:321–30.
88. Kwon Y, Lee SJ, Lee E, Kim D, Park D. BetaPix heterozygous mice have defects in neuronal morphology and social interaction. *Biochem Biophys Res Commun*. 2019;516:1204–10.
89. Varshini MS, Reddy RA, Krishnamurthy PT, Wadhvani A. Harmony of Wnt pathway in Alzheimer's: navigating the multidimensional progression from preclinical to clinical stages. *Neurosci Biobehav Rev*. 2024;165:105863.
90. Inestrosa NC, Varela-Nallar L. Wnt signaling in the nervous system and in Alzheimer's disease. *J Mol Cell Biol*. 2014;6:64–74.
91. Cao M, Pu T, Wang L, Marshall C, He H, Hu G, et al. Early enriched physical environment reverses impairments of the hippocampus, but not medial prefrontal cortex, of socially-isolated mice. *Brain Behav Immun*. 2017;64:232–43.
92. Xie Y, Liu J, Hou Z, Wang H, Liu K, Chen X, et al. CD4-derived double-negative T cells ameliorate Alzheimer's disease-like phenotypes in the 5xFAD mouse model. *CNS Neurosci Ther*. 2025;31:e70187.
93. Igarashi H, Ueki S, Kitaura H, Kera T, Ohno K, Ohkubo M et al. Longitudinal GluCEST MRI changes and cerebral blood flow in 5xFAD mice. *Contrast Media Mol Imaging*. 2020;2020:8831936.
94. Wang Z, Zhang Y, Feng W, Pang Y, Chen S, Ding S, et al. Miconazole promotes cooperative ability of a mouse model of Alzheimer disease. *Int J Neuropsychopharmacol*. 2022;25:951–67.
95. Zhang Y, Pang Y, Feng W, Jin Y, Chen S, Ding S, et al. miR-124 regulates early isolation-induced social abnormalities via inhibiting myelinogenesis in the medial prefrontal cortex. *Cell Mol Life Sci*. 2022;79:507.
96. Potemkin N, Cawood SMF, Guevremont D, Mockett B, Treece J, Stanton JL, et al. Whole transcriptome RNA-Seq reveals drivers of pathological dysfunction in a transgenic model of Alzheimer's disease. *Mol Neurobiol*. 2025. <https://doi.org/10.1007/s12035-025-04878-6>
97. Rolls ET. Emotion, motivation, decision-making, the orbitofrontal cortex, anterior cingulate cortex, and the amygdala. *Brain Struct Funct*. 2023;228:1201–57.
98. Apps MA, Rushworth MF, Chang SW. The anterior cingulate gyrus and social cognition: tracking the motivation of others. *Neuron*. 2016;90:692–707.
99. Stolz DS, Muller-Pinzler L, Krach S, Paulus FM. Internal control beliefs shape positive affect and associated neural dynamics during outcome valuation. *Nat Commun*. 2020;11:1230.

Publisher's note

Springer Nature remains neutral with regard to jurisdictional claims in published maps and institutional affiliations.